

**Life Time Studies of
Irradiated LEDs and VCSELs
for the ATLAS Experiment at the
Large Hadron Collider**

Diplomarbeit

der Philosophisch-naturwissenschaftlichen Fakultät
der Universität Bern

vorgelegt von

Remigius K. Mommsen

1997

Leiter der Arbeit: Prof. Dr. K. Pretzl
Laboratorium für Hochenergiephysik

Abstract

In this diploma thesis results of life time studies of irradiated Light Emitting Diodes (LEDs) and Vertical Cavity Surface Emitting Laser diodes (VCSELs) are presented. Following the encouraging results obtained in a previous life time test of neutron irradiated LEDs, we built an automatic measurement system in order to make long term tests with a large number of irradiated devices feasible. After the irradiation of about 250 LEDs from two different manufacturers and about 200 VCSELs with the high fluences anticipated for the inner tracker of ATLAS, we report on the radiation damage and the conditions required for its annealing. The life time after irradiation was investigated by operating the devices at an elevated temperature of 50°C for several months, resulting in operating times corresponding to up to 45 years of LHC running.

This work is dedicated to my parents
who died much too early for partici-
pating in the outcome of their efforts.

Contents

| | | |
|----------|---|-----------|
| 1 | Introduction | 1 |
| 2 | The ATLAS Detector at LHC | 3 |
| 2.1 | Introduction | 3 |
| 2.2 | The ATLAS Layout | 3 |
| 2.3 | The Inner Detector of ATLAS | 6 |
| 2.3.1 | Layout | 6 |
| 2.3.2 | Radiation Environment | 8 |
| 2.4 | Data Transmission for the SCT | 8 |
| 3 | Irradiation of LEDs | 11 |
| 3.1 | Overview | 11 |
| 3.2 | Radiation Damage in Semiconductors | 11 |
| 3.2.1 | Displacement Effects | 12 |
| 3.2.2 | Non-Ionizing Energy Loss | 13 |
| 3.2.3 | Damage Constants | 14 |
| 3.3 | Annealing | 15 |
| 4 | Experimental Procedure | 17 |
| 4.1 | Introduction | 17 |
| 4.2 | The Scanning Machine | 17 |
| 4.2.1 | Layout | 19 |
| 4.2.2 | Hardware | 20 |
| 4.2.3 | Online Software | 22 |
| 4.2.4 | Offline Software | 24 |
| 4.3 | Measurement Algorithm | 25 |
| 4.3.1 | The Standard Measurement | 26 |
| 4.3.2 | The Special Measurements | 26 |
| 4.3.2.1 | I-V and L-I scans | 26 |
| 4.3.2.2 | Light Cone Scans | 27 |
| 4.3.2.3 | Position of the Maximal Light Output | 27 |
| 4.3.3 | The Normalization of the Light Output | 28 |
| 4.3.4 | Light Output into an Optical Fibre | 29 |
| 4.4 | Irradiation | 29 |

| | | |
|----------|--|-----------|
| 5 | Devices | 33 |
| 5.1 | Overview | 33 |
| 5.2 | Light Emitting Diodes (LEDs) | 33 |
| 5.2.1 | ABB Hafo LEDs | 37 |
| 5.2.2 | GEC-Marconi LEDs | 37 |
| 5.3 | Vertical Cavity Surface Emitting Lasers (VCSELs) | 38 |
| 5.3.1 | Temperature Dependence of the Lasing Threshold Current | 39 |
| 5.3.2 | Modal Noise in the Laser Cavity | 39 |
| 6 | Short Term Results | 43 |
| 6.1 | Introduction | 43 |
| 6.2 | Damage Constants for GEC-Marconi LEDs | 43 |
| 6.3 | Annealing | 45 |
| 6.3.1 | ABB Hafo LEDs | 45 |
| 6.3.2 | GEC-Marconi LEDs | 46 |
| 6.3.3 | VCSELs | 46 |
| 6.4 | Temperature Dependence of Annealing | 47 |
| 6.5 | Summary | 48 |
| 6.6 | Behavior of Failing Devices | 50 |
| 7 | Long Term Results | 55 |
| 7.1 | Introduction | 55 |
| 7.2 | The Acceleration of Aging | 55 |
| 7.3 | Life Time of Irradiated LEDs and VCSELs | 56 |
| 7.4 | Long Term Stability | 59 |
| 8 | Summary and Outlook | 61 |
| | Bibliography | 63 |
| | Acknowledgments | 69 |

List of Figures

| | | |
|-----|--|----|
| 2.1 | Layout of the Large Hadron Collider (LHC) | 4 |
| 2.2 | View of the ATLAS detector in the underground hall | 4 |
| 2.3 | View of the ATLAS calorimeter system | 5 |
| 2.4 | A cross-section of the inner detector layout | 7 |
| 2.5 | Charged hadron fluence in the inner detector | 8 |
| 2.6 | Neutron fluence in the inner detector | 8 |
| 2.7 | Schematic of the data transmission system | 9 |
| | | |
| 4.1 | The Scanning Machine installed in the laboratory | 18 |
| 4.2 | Longitudinal sectional view of the scanning machine | 18 |
| 4.3 | Temperature controlled support with eight modules installed | 19 |
| 4.4 | Schematic layout of the data acquisition hardware used for the scanning machine | 21 |
| 4.5 | Schematic overview of the data and control flow between the different components of the DAQ system | 23 |
| 4.6 | Schematic data flow for the offline processing | 25 |
| 4.7 | Sample of a light cone scan | 27 |
| 4.8 | Neutron energy spectrum at the RAL ISIS facility | 31 |
| | | |
| 5.1 | Devices mounted on ceramic boards | 35 |
| 5.2 | Distribution of the light output at +10°C of the ABB Hafo and GEC-Marconi LEDs | 37 |
| 5.3 | Sketch of an oxide-confined VCSEL | 39 |
| 5.4 | L-I curve with and without modal noise from feedback | 40 |
| 5.5 | Single mode vs. multi mode behavior of VCSELs | 41 |
| | | |
| 6.1 | Damage function fit for GEC-Marconi LEDs | 44 |
| 6.2 | Typical annealing of ABB Hafo LEDs | 46 |
| 6.3 | Annealing behaviors of GEC-Marconi LEDs | 47 |
| 6.4 | Annealing of VCSELs | 48 |
| 6.5 | Temperature dependence of annealing | 49 |
| 6.6 | Relative light output of individual LEDs and VCSELs after the irradiation as a function of fluence | 51 |
| 6.7 | Examples of failing LEDs | 52 |
| | | |
| 7.1 | Acceleration factors for different thermal activation energies | 56 |
| 7.2 | Long term stability of LEDs | 59 |

Chapter 1

Introduction

In 1994 the European Organization for Nuclear Research (CERN) approved the Large Hadron Collider (LHC) [1], a new proton-proton collider with a center of mass energy of 14 TeV, which will be operational in the year 2005. This accelerator will give the opportunity to experimentally verify our understanding of elementary particle physics at the TeV scale and to search for new predicted particles like the Higgs boson and super-symmetric particles.

The ATLAS detector is one of the four detectors to be built at LHC. It will be a general purpose proton-proton detector designed to exploit the full discovery potential of LHC.

The work presented here concerns the data transmission to and from the Semiconductor Tracker (SCT) of ATLAS. One of the technologies proposed for the data read-out of the SCT uses optical links based on Light Emitting Diodes (LEDs) or, as an alternative, on Vertical Cavity Surface Emitting Lasers (VCSELs). Mounted close to the detector modules, these devices will be subject to high fluences on the order of 10^{14} charged hadrons and 10^{14} neutrons per cm^2 during ten years of LHC operation.

While it is well known, that the light output of LEDs may decrease after the irradiation, little information is available about the aging properties and the life time of irradiated LEDs. The VCSEL technology emerged recently and is still in development. Therefore, there are only a few studies on the long term stability of VCSELs available. The same is obviously true for the radiation hardness and life time of irradiated VCSELs.

A previous life time test of a small sample of GaAlAs LEDs (manufactured by ABB Hafo) irradiated with up to $1.4 \cdot 10^{14}$ n/cm² was performed earlier [2, 3]. In that test the devices showed an almost complete annealing of radiation induced defects after the irradiation, and five LEDs were operated in an accelerated life time test without seeing any degradation for a duration which is estimated to correspond to about 57 years of operation in the ATLAS SCT.

Although these results are very encouraging, higher statistics are necessary in order to predict the reliability of LEDs used in the SCT, and the conditions required for the annealing have to be clarified. Additionally, the assumption that ionization effects due to charged particles are negligible has to be confirmed. For this purpose,

the irradiation was not only done with neutrons, but also with protons. In order to make the measurement of a large number of devices feasible, an automatic measurement system (the scanning machine) for up to 448 LEDs or VCSELs was built.

After this introduction, the ATLAS detector and the data transmission system for the SCT will be described in chapter 2. Irradiation effects in semiconductors and the annealing of radiation induced defects will be discussed in chapter 3. The scanning machine will be presented in chapter 4 and the devices used in this test are described in chapter 5. The last two chapters present the results obtained from the irradiation studies: in chapter 6 the short term annealing will be described and in chapter 7 the long term behavior during the accelerated aging will be discussed.

Chapter 2

The ATLAS Detector at LHC

2.1 Introduction

The Large Hadron Collider [1] is a proton-proton collider operating at a center of mass energy of $\sqrt{s} = 14 \text{ TeV}$ and at a design luminosity of $\mathcal{L} = 10^{34} \text{ cm}^{-2} \text{ s}^{-1}$. It is located at the *Centre Europeen de la Recherche Nucleaire* (CERN) in Geneva, Switzerland, and will be operational in the year 2005. Figure 2.1 shows the layout of the LHC and the approximate location of the four main experiments ATLAS [4], CMS [5], LHC-B [6] and ALICE [7]. In addition to its main function as a proton-proton collider, LHC will provide heavy ion (Pb) collisions at a center of mass energy of more than 10^3 TeV and at a luminosity of about $2 \cdot 10^{27} \text{ cm}^{-2} \text{ s}^{-1}$.

The ATLAS detector design with its main components — the muon spectrometer, the electromagnetic and hadronic calorimeter, the inner detector and the trigger system — is described in the Technical Proposal [4] and, in much more detail, in the Technical Design Reports (TDR) which will be published mostly in 1997.

2.2 The ATLAS Layout

The ATLAS detector is designed to exploit the full discovery potential of LHC. Its layout is governed by the following criteria:

- very good electromagnetic calorimetry for electron and photon identification and measurements, complemented by hermetic jet and missing E_T calorimetry;
- efficient tracking at high luminosity for lepton momentum measurements, for b-quark tagging, and for enhanced electron and photon identification, as well as tau and heavy-flavor vertexing and reconstruction capability of some B decay final states at lower luminosity;
- stand-alone, precision, muon-momentum measurements up to the highest luminosity, and very low- p_T trigger capability at lower luminosity.

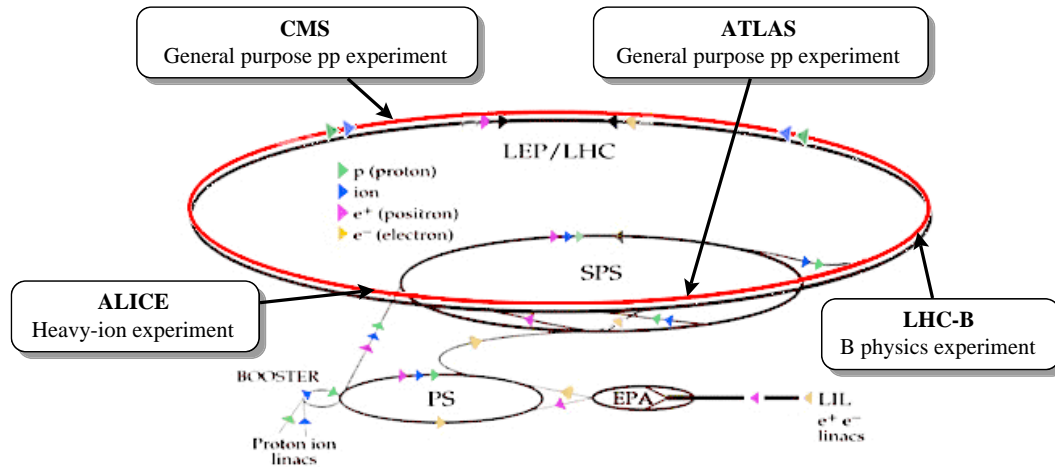


Figure 2.1: Layout of the Large Hadron Collider (LHC) and approximate location of the four main experiments ATLAS, CMS, LHC-B and ALICE

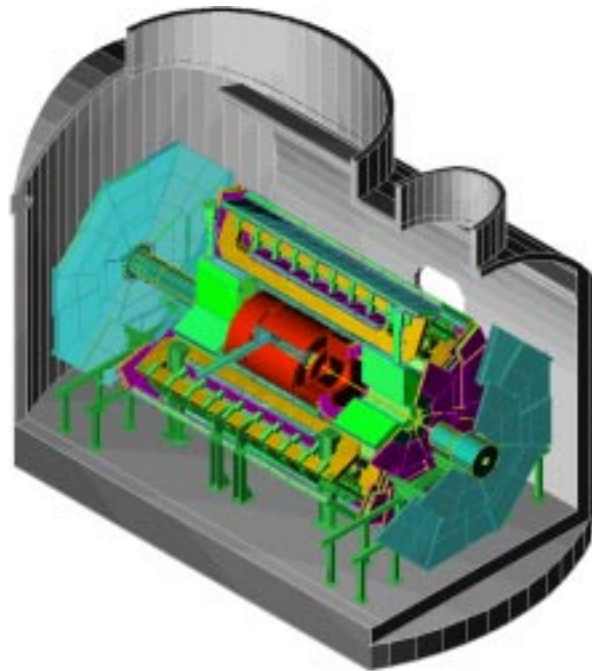


Figure 2.2: View of the ATLAS detector in the underground hall [4]

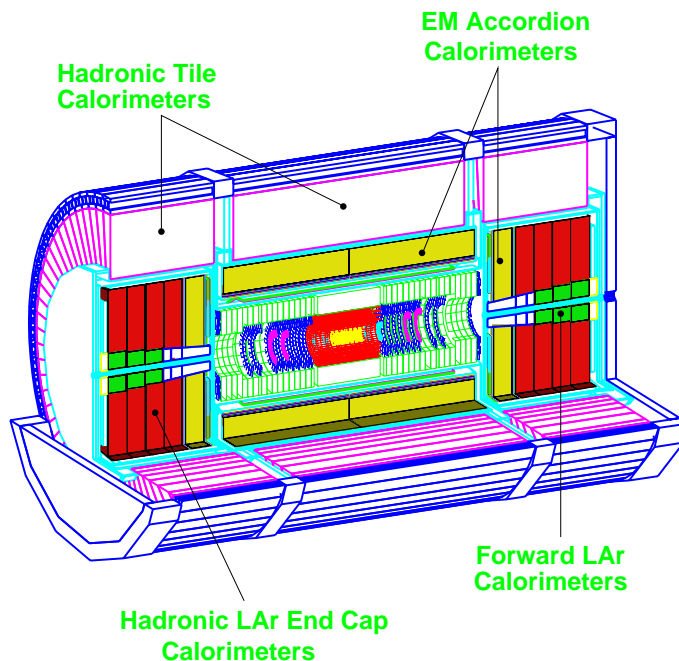


Figure 2.3: View of the ATLAS calorimeter system [4]

The overall detector layout is shown in figures 2.2 and 2.3. With an overall length of ~ 42 m, a diameter of ~ 22 m and a weight of ~ 7000 tons, the ATLAS detector is huge even if compared to the largest of today’s high energy experiments.

The magnet configuration is based on two different magnet systems, namely the super-conducting solenoid around the inner detector cavity and large superconducting air-core toroids outside the calorimetry for the muon system. This magnet layout provides a high-resolution, large-acceptance and robust stand-alone muon spectrometer and gives little constraints on the calorimetry and the inner detector.

The inner detector is contained in a 6.80 m long cylinder with a radius of 1.15 m surrounded by a 5.3 m long super-conducting solenoid providing a 2 T axial field for tracking. Pattern recognition, momentum measurement and vertex detection, as well as enhanced electron identification are achieved with discrete high-resolution pixel and strip detectors in the inner part and with a continuous straw-tube tracker with an integrated transition radiation detector (TRT) in the outer part (cf. section 2.3).

The electromagnetic and the hadronic calorimetry occupy the radial space from 1.15 m to 4.23 m. The electromagnetic section uses lead absorbers and liquid argon (LAr) as active medium. It is implemented in an “accordion” geometry, both for the barrel ($|\eta| < 1.4$) and for the end-caps ($1.4 < |\eta| < 3.2$)¹. The hadronic calorimeter in the barrel region is built up by scintillator and iron absorber tiles

¹Directions inside the ATLAS detector are parameterized by the pseudo rapidity $\eta = -\ln \tan(\theta/2)$ where θ denotes the polar angle. The plane perpendicular to the beam direction is parameterized by the radius r and the azimuthal angle ϕ .

placed perpendicular to the beam axis. The readout is done by wavelength-shifting fibers coupled radially to the scintillator planes. This layout combines simple, low-cost construction with a good performance. At larger rapidity, where higher radiation resistance is required, the hadronic calorimeter is based on liquid argon as active material. For $1.5 < |\eta| < 3.2$ parallel copper plates are used as absorbers. For the highest rapidity region covering $3.2 < |\eta| < 4.9$ a dense forward calorimeter is used. The whole calorimetry system provides very good jet and E_T^{miss} performance of the detector.

The ATLAS calorimeters are surrounded by the muon system. The air-core toroid system provides a large field volume with strong bending power combined with a light and open structure. Therefore, multiple scattering effects are minimized and an excellent muon momentum resolution is achieved with three stations of high-precision tracking chambers. In addition, fast trigger chambers are used for a stand-alone muon-trigger.

2.3 The Inner Detector of ATLAS

2.3.1 Layout

The Inner Detector (ID) of ATLAS will be used to reconstruct the tracks and any vertices in an event with high efficiency, and it contributes together with the calorimeter and the muon systems to the muon, electron and gamma identification.

To achieve this performance, the ID combines high-resolution detectors at the inner radii with continuous tracking elements at outer radii. The former consist of the SemiConductor Tracker (SCT) using silicon microstrip technology, and high granularity silicon pixel detectors. The total number of precision layers is limited by the power dissipation and the high cost of the readout electronics. Therefore, in the outer part, the tracking is done with the Transition Radiation Tracker (TRT), which provides a large number of tracking points with much less material per point and at lower cost. The combination of these two techniques gives a robust pattern recognition. In addition, the electron identification capabilities are enhanced by the detection of transition radiation photons in the straw tubes.

Figure 2.3.1 shows the arrangement of the detectors inside one quarter of the barrel part, and one of the two identical forward parts on both sides. The SCT is contained within a radius of 60 cm, followed by the TRT and the general support and service area at the outermost radius.

The barrel consists of six detector layers arranged on concentric cylinders around the beam axis covering the region with $|\eta| < 1$. The forward detectors are mounted on disks perpendicular to the beam axis and cover the rapidity region up to $|\eta| < 2.5$. In the barrel TRT the straws are parallel to the beam axis, and in the forward TRT the straws run in radial directions.

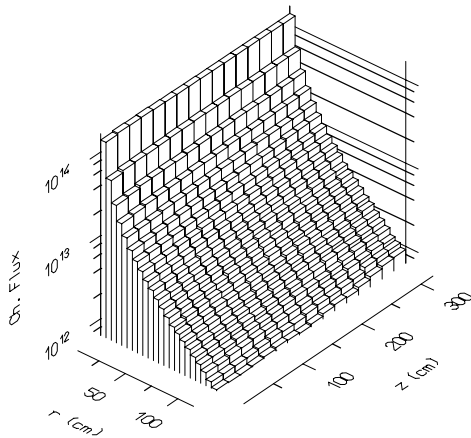


Figure 2.5: Charged hadron fluence ($\text{cm}^{-2} \text{yr}^{-1}$) in the inner detector [4]

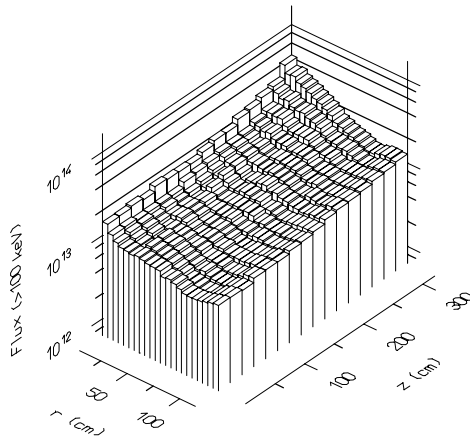


Figure 2.6: Neutron ($E > 100 \text{ keV}$) fluence ($\text{cm}^{-2} \text{yr}^{-1}$) in the inner detector [4]

2.3.2 Radiation Environment

The inner detector of ATLAS is exposed to intense fluences of neutral and charged hadrons produced in the primary p-p interactions, and albedo neutrons backscattered from the calorimeters. Close to the interaction point, the particle flux is dominated by charged hadrons (mainly pions) which exhibits a typical $1/r^2$ dependence, where r is the distance from the beam axis, as shown in figure 2.5. Such a behavior is expected for the fluence of particles generated at the interaction point with the expected flat $dN/d\eta$ distribution, where N denotes the number of charged particles produced. At larger radii the fluence of neutrons dominates (cf. fig. 2.6). These neutrons are scattered many times before being captured and give rise to a relatively uniform and isotropic “gas” with typical kinetic energies of $\sim 1 \text{ MeV}$.

2.4 Data Transmission for the SCT

One SCT detector module consists of two hybrids serving each six microstrip detectors with 128 read-out channels per detector. The hybrids are placed on both sides of the detector module. The data rate to be read-out from one detector module, i.e. two hybrids, is approximately 35 Mb/s. Each SCT module requires also a data link for synchronization with the collider (40 MHz bunch crossing clock) and for trigger and control. Obviously, the data links have to be operational for the full life time of ATLAS, i.e. during ten years, and the material introduced to the inner detector should be kept as low as possible.

One attractive solution for the data transmission is based on fibre optic links. This system will be described below. An alternative system is based on miniature shielded twisted pair cables as proposed for the TRT. It has advantages in cost and radiation hardness over the optical system, but it lacks the desired electrical isolation and introduces more material into the inner detector.

Figure 2.7: Schematic of the data transmission system showing data flow and redundancy (adapted from [8])

Figure 2.7 gives an overview of the optical data transmission system. It consists of three optical fibres per detector module, two for the data readout and one for multiplexed trigger, timing and control (TTC) signals. The two readout links operate at 40 Mb/s each, providing headroom and redundancy for the data readout. The SCT will consist of 4088 detector modules, i.e. there will be a total of 12264 fibres leading from the SCT to the counting room.

The data is sent from the SCT detector module through a short flat cable to a nearby optical hybrid, where the electrical signal is converted to an optical one by LEDs driven by the LED Driver Chip (LDC). The LDC provides two completely independent circuits, both capable to generate a forward current from zero to 50 mA. Although the normal operating current for the GEC-Marconi LEDs is 20 mA, higher currents are needed for the annealing of radiation damage (cf. chapter 6).

As an alternative to GEC-Marconi LEDs, Vertical Cavity Surface Emitting Lasers (VCSELs) could be used. However, VCSELs are a very new device type still under development. For more information about the LEDs and VCSELs proposed for the optical links see chapter 5.

The trigger, clock and command signals are received by a PIN diode and are demultiplexed by the DORIC3 chip. Two sets of clock and command outputs are available. The normal outputs drive the local detector module and the spare outputs are fed into the adjacent detector module. Both output-paths can be switched on and off independently by means of command signals. Therefore, the loss of one TTC link can be compensated by the adjacent one, which provides some redundancy.

The three fibres from each detector module will be merged into 12-fold radiation hard fibre ribbons going to optical patch panels between the calorimeters. At this point the transition to non-radiation hard fibres will be made. These fibres are running to off-detector Read-Out Driver modules (RODs), where the optical signals are reconverted into electrical signals by means of high responsivity silicon PIN diodes. The optical TTC signals will be produced by a LED in the same ROD and sent to the detector.

The major worry concerning the optical data transmission system arises from the high radiation level in the inner detector (cf. section 2.3.2) imposing high demands on radiation hardness of the electronics used inside the detector, which applies also for the components of the optical links. Beside the LED/VCSEL irradiation tests described in this work, extensive measurements on several types of fibres at high gamma-ray and neutron fluences have been done for commercially available multi mode and mono mode fibres [9, 10, 11, 12]. Preliminary irradiation tests of PIN diodes have been done as well and further tests are in progress [13, 14].

Chapter 3

Irradiation of LEDs

3.1 Overview

In this section a short summary of radiation effects in semiconductors will be given. This issue becomes more important at LHC with its significantly increased luminosity compared to already operational accelerators. Additionally, the signal-processing electronic is integrated closer to the detectors and therefore close to the interaction point.

3.2 Radiation Damage in Semiconductors

In spite of the complex interactions of radiation with matter, the interaction of high energy particles with semiconductors can be classified in three types of effects, as described very nicely in [3, 15]:

1. Transient ionization effects. These are the manifestations of electron-hole pairs created by ionizing interactions and may lead to radiation-induced photocurrents. These effects are very short living and are used to detect the passage of particles. However, they may lead to single event up-sets in devices relying on low currents like PIN photodiodes, for example.
2. Long-term ionization effects. The electron-hole pairs produced by ionization in insulators can not recombine as easily as in the semi-conductor material. This leads to a large concentration of trapping centers and therefore to space-charge build-up. Space-charge build-up is mainly a problem in devices relying on insulators or di-electrics where it is revealed by a threshold voltage shift. The large concentration of trapping centers may also influence the optical absorption characteristics.
3. Displacement effects (also called bulk damage). These are the manifestations of the displacement of atoms from their normal sites in the crystal lattice. It may be caused both by neutral and by charged particles, although for the latter ionization is the primary effect. Bulk damage may also be caused by photons

through high energy electrons created by photo effect, Compton scattering or pair production. Because the degradation of LEDs is primarily caused by displacement effects, it will be described in more detail in the following section.

3.2.1 Displacement Effects

The displacement damage, also called bulk damage, cannot be measured directly. It must be determined by measurements of the defect concentration after irradiation or the impact of these defects on material properties. The generation of displacement damage can be described in four steps:

1. The incident particle collides with an atom of the semiconductor, the so called Primary Knock-on Atom (PKA). The energy required to knock it out of its lattice site is ~ 25 eV in Si and ~ 10 eV in GaAs [16, 17]. In the case of high energy nuclear particles, the collisions may be sufficiently violent to undergo a nuclear reaction, resulting in a number of fragments of the target atom and possibly other secondary particles.
2. The PKA will rapidly loose its energy in the vicinity of the primary interaction site due to both ionization and the displacement of further atoms, eventually producing a cascade of collision processes. The structure of the defects produced in silicon by a single PKA was simulated by several authors [18, 19, 20]. A tree-like structure of relatively isolated Frenkel pairs with terminal subclusters with a large density of vacancies and interstitials was found. This is due to the increasing elastic scattering cross section at collision energies below ~ 10 keV. These results seem in agreement with transmission electron microscopy studies, where no evidence for larger disordered regions was found in neutron irradiated silicon [21].
3. After the initial displacement damage occurred during the short collision time scale of about 10^{-14} s to 10^{-12} s [19], thermally activated motion causes rearrangements of the lattice defects and a considerable amount of annealing at room temperature takes place. This short term annealing occurs typically in less than one second. Some of this rearrangement is influenced by impurities present in the material prior to irradiation.
4. The thermally stable defects, including di-vacancies, vacancy-impurity complexes and larger clusters, influence the properties of the semiconductor material and thus of the device function. The nature of these defects can be investigated e.g. with Deep Level Transient Spectroscopy (DLTS) [22, 23].

3.2.2 Non-Ionizing Energy Loss

The different defect types introduced by the bulk damage might be expected to have different probabilities for their formation depending on the type and energy of the incident particle. However, it has been observed that the degradation due to displacement damage of a given semiconductor device is primarily a function of the non-ionizing energy loss (NIEL). This observation (commonly referred to as the NIEL hypothesis) implies that the defects produced act as individual atomic defects [21, 24]. Although some deviations of measured device degradation from the one expected according to the NIEL hypothesis have been reported [25]–[27], the NIEL hypothesis has been verified experimentally over a wide range of energies, for different incident particles, for silicon and to a somewhat less degree for GaAs [25]–[30].

The NIEL for a particle passing through matter is given by [31]

$$\frac{dE}{dx} = \sum_{Z,A} \int E_r \frac{N_a}{A'} \frac{d\sigma}{dE_r} L(E_r) dE_r \quad (3.1)$$

where N_a and A' are Avogadro's number and the atomic weight of the medium, $d\sigma/dE_r$ is the differential cross section to produce a recoil fragment with energy E_r of atomic weight A and atomic number Z , and the function $L(E_r)$ is the Lindhard partition function [32], which gives the fraction of the recoil energy E_r that contributes to displacement damage.

Extensive calculations have been performed for silicon [17, 28, 33, 34] and for neutrons in GaAs [17, 28]. The authors in [31] used these results to calculate the NIEL in GaAs for ISIS neutrons and for 24 GeV protons. Table 3.1 summarizes their results and gives relative NIEL values compared to 1 MeV neutrons.

| Irradiation type | 1 MeV neutrons | | ISIS ^a neutrons | | 24 GeV protons | | 300 MeV pions | |
|-------------------------------|----------------|------|----------------------------|------|----------------|------|---------------|------|
| | Si | GaAs | Si | GaAs | Si | GaAs | Si | GaAs |
| NIEL (keV cm ² /g) | 1.7 | 0.55 | 2.0 | 0.9 | 1.0 | 2.9 | 1.9 | 3.6 |
| Ratio to 1 MeV neutrons | 1.0 | 1.0 | 1.2 | 1.6 | 0.59 | 5.3 | 1.1 | 6.5 |
| Ratio to 24 GeV protons | 1.7 | 0.2 | 2.0 | 0.3 | 1.0 | 1.0 | 1.9 | 1.2 |

Table 3.1: NIEL values for Si and GaAs for different particles and energies from [31] and references given therein. The accuracy of NIEL for neutrons is $\sim 10\%$ and for protons uncertainties on the order of a factor of 2 are not unlikely.

^aThe irradiation facility at the Rutherford Appleton Laboratory (RAL) is called ISIS. The neutron energy spectrum is shown in figure 4.8.

3.2.3 Damage Constants

The radiation induced displacement damage may introduce additional states within the forbidden bandgap of the semiconductor. They act as nonradiative recombination centers competing with radiative centers for minority carriers. Therefore, the minority carrier lifetime τ is reduced by [35]

$$\frac{1}{\tau} = \frac{1}{\tau_0} + \sum_i v_{th} \sigma_i n_i \quad (3.2)$$

where τ_0 denotes the pre-irradiation minority carrier lifetime, v_{th} the average thermal velocity of the minority carriers, n_i and σ_i the density and capture cross section, respectively, of the recombination centers of a given type i , and the sum extends over the different types of radiation induced defects. As long as there is no significant overlap of the defect regions produced by the individual incident particles, the initial defect density will be proportional to the particle fluence ϕ :

$$n_i = c_i \phi \quad (3.3)$$

where the coefficient c_i stands for the density of particular defects per unit fluence. Defining a damage constant K ,

$$K \equiv v_{th} \sum_i c_i \sigma_i \quad (3.4)$$

equation 3.2 can be written as

$$\frac{\tau_0}{\tau} = 1 + \tau_0 K \phi \quad (3.5)$$

The ratio τ_0/τ of the minority carrier lifetime before and after the irradiation can be related to the relative light output after irradiation assuming that the total current density in the junction is dominated by diffusion currents [36]:

$$\left(\frac{P_0}{P}\right)^{\frac{2}{3}} = \frac{\tau_0}{\tau} \quad (3.6)$$

Thus, the parameter $k \equiv \tau_0 K$ can be calculated from the relative light output (RLO) of the devices after the irradiation with a total particle fluence ϕ :

$$\left(\frac{1}{RLO}\right)^{\frac{2}{3}} = \left(\frac{P_0}{P}\right)^{\frac{2}{3}} = 1 + k \phi \quad (3.7)$$

Therefore, if the product $k\phi$ is significant compared to 1, the light output will decrease substantially. According to the NIEL hypothesis, one expects that k scales with the NIEL (cf. section 3.2.2). In section 6.2 the parameter k will be determined for ISIS neutrons and 24 GeV protons from our data. The result obtained supports the NIEL hypotheses and agrees well with the NIEL ratios given in table 3.1.

During the annealing (cf. section 3.3), the different defect concentrations will change: some are repaired by current injection, others recombine to stable defect clusters. Therefore, the damage parameter k will change during the annealing (cf. section 6.2).

3.3 Annealing

Defects which are stable at room temperature may be annealed under forward current (injection annealing), because electron-hole recombinations at a defect can increase the defect's mobility. For the same reason, less degradation may be observed for open-circuit irradiation than for short-circuit irradiation or for irradiation under reverse bias, since in the former case the electron-hole pairs generated during the irradiation recombine within the device and may contribute to the annealing [37].

Thermal annealing of LEDs was reported, but it seems to require a temperature above 200°C for the annealing of defects which are stable at room temperature [16, 38].

Chapter 4

Experimental Procedure

4.1 Introduction

The aim of the present work is to investigate the impact of radiation induced defects on the light output and the life time of a large number of LEDs and VCSELs. For this purpose, an automatic measurement system, called the scanning machine, was built. Before the irradiation, the devices were temporarily installed in the scanning machine for measuring the light output as a function of the forward current and the operating temperature. Some of the LEDs were subjected to a burn-in treatment at 50 mA and 50°C before the irradiation. After the irradiation, the devices were reinstalled in the scanning machine. After a first measurement at the default conditions (cf. table 5.2), the devices were operated at different forward currents and at either +10°C or -10°C for several days or weeks in order to investigate the annealing behavior. For the estimation of the reliability of the irradiated devices, the devices were operated for several months at an elevated temperature of 50°C in order to accelerate the aging.

4.2 The Scanning Machine

In the previous life time test of irradiated LEDs [2, 3] measurements were made with a semi-automatic measurement system on expensive pigtailed devices where the use of optical patch cables implied a lot of manual work. In order to avoid this kind of problems, in the present study unpackaged devices were tested without using optical fibres by moving an optical receiver directly in front of the devices. This procedure allowed the construction of a fully automatic system, called the scanning machine. It provides space and driver circuits for 448 LEDs or VCSELs. A picture of the scanning machine with its electronics and with the data acquisition system is shown in figure 4.1.

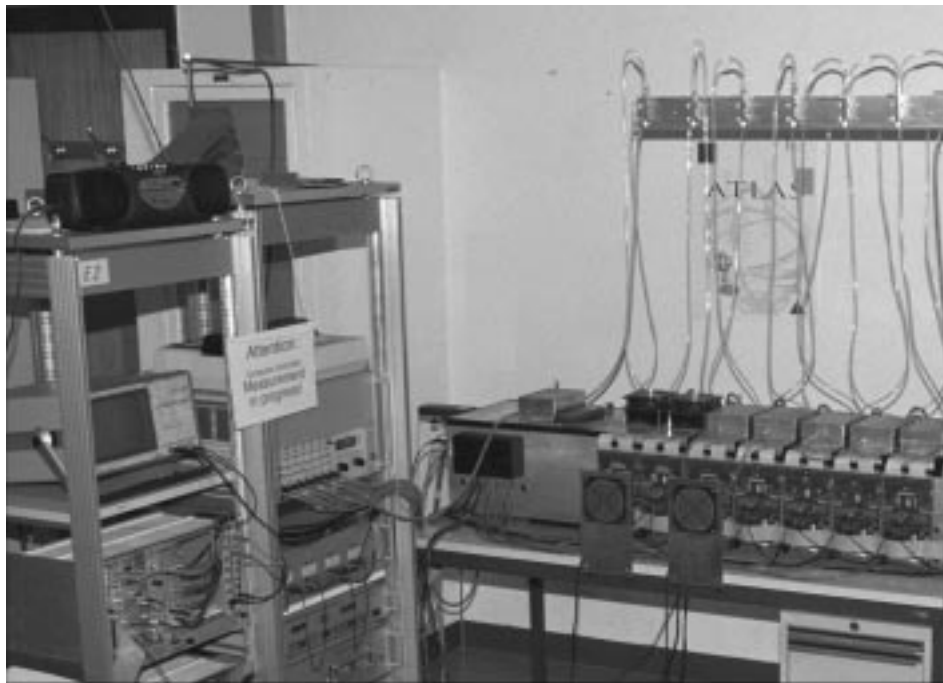


Figure 4.1: The Scanning Machine installed in the laboratory (right) and its associated electronics (left)

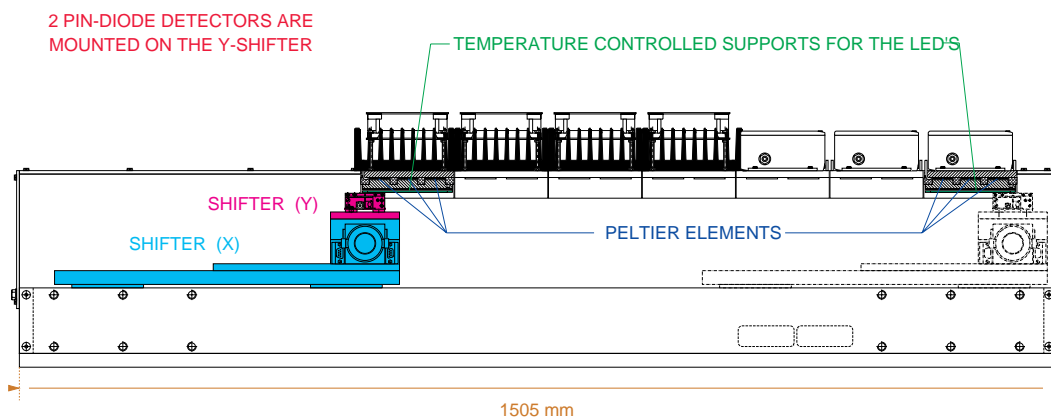


Figure 4.2: Longitudinal sectional view of the scanning machine with the longitudinal (x) and transverse (y) shifter. The shifter moving in the longitudinal direction is shown both at the leftmost (shaded) and at the rightmost (dashed lines) position. The transverse shifter carries two PIN diodes and receiver boards.

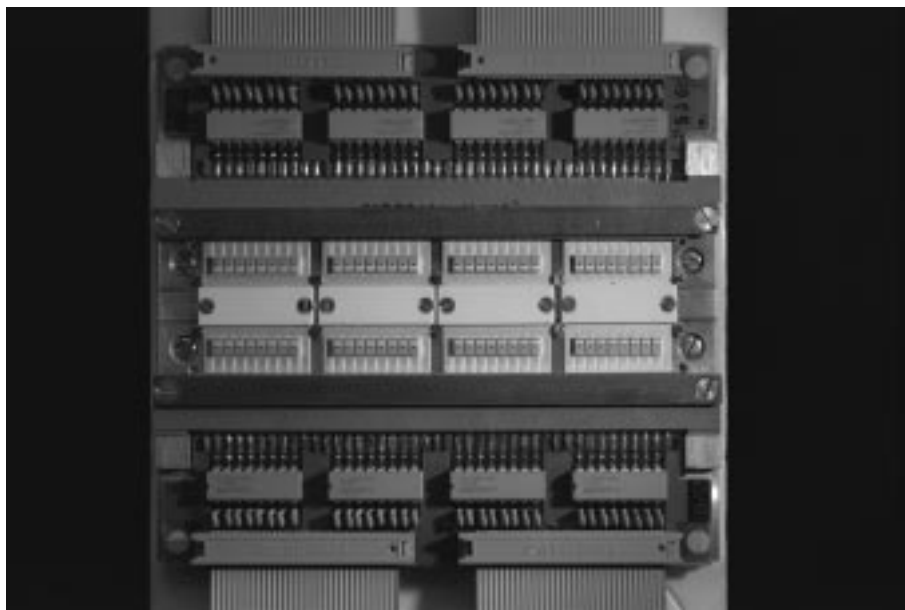


Figure 4.3: Temperature controlled support (block) with eight modules installed, each one carrying eight ABB Hafo LEDs

4.2.1 Layout

A longitudinal view of the scanning machine is shown in figure 4.2. It is based on two shifters running in the longitudinal and transverse direction, respectively. The transverse shifter carries two optical receiver boards, each with an individual PIN photodiode, which is placed at a distance of a few mm from the LEDs. By moving the PIN diode to the position yielding the maximum signal below a given LED, the measurement of the light output is reproducible to a few percent.

Eight LEDs or one 20-fold VCSEL array are mounted together on one ceramic board, called *module*. A picture of a module for each type of device is shown in figure 5.1. Modules are mounted in groups of eight on temperature controlled supports, called *blocks* (shown in figure 4.3), facing downwards to the PIN diode. The modules provide the electrical, mechanical and thermal contact of the LED or VCSELs with the block. The electrical contact is achieved by special connectors to passive electronics boards for signal termination, and from there via flat ribbon cables to the driver boards located outside of the scanning machine. The mechanical fixation consists of two guiding screws, defining the sideward position, and of the electrical connector with a precise counterpart pressing the module on the support block. This construction allows for easy mounting and dismantling of the modules and assures a sufficiently reproducible positioning of the LEDs before and after the irradiation. The distance between the LED and the PIN diode is defined by mechanical pieces which can be adjusted for each block as needed.

In the scanning machine, there is space for seven temperature blocks. Each one can be set individually to a temperature ranging from -10°C to 50°C , using

Peltier elements for cooling or heating. In order to protect the LEDs from ice and condensation, the humidity inside the scanning machine must be kept low. Therefore, the scanning machine provides a tight volume with a nitrogen atmosphere.

Each LED has its own computer controlled driver circuit which allows to set the forward current between 0 mA and 100 mA, and to switch individual LEDs on, off or to pulsed mode.

4.2.2 Hardware

A schematic layout of the data acquisition hardware used for the scanning machine is shown in figure 4.4. The hardware consists of a VME crate housing an OS/9 system, a Greenspring 16-bit ADC card, and a GPIB interface for remote control of a LeCroy 9450 digital 350 MHz oscilloscope. The operating parameters such as PIN diode position, LED forward current and continuous or pulsed operating mode are transmitted via CAMAC input/output registers on a simple bus system (HEBus) developed at the University of Bern.

The measurement of the LED characteristics and of the operating temperature of the devices is performed by the 16-bit ADC card via an ADC adapter placed in a NIM crate. The ADC adapter provides suitable connectors and filtering for the different input paths. The oscilloscope is used for fall and rise time measurement of LEDs.

In the following, the main parts of the hardware will be described. The PIN diodes is moved by two shifters to the LED/VCSEL of interest in order to measure the light output. The measured signal is amplified and converted by the ADC. In order to eliminate fast noise the signal is filtered before it is fed into the ADC. The electronic boards supply the DC or pulsed current for the operation of the LEDs/VCSELs and provide multiplexing of the forward voltage and current of the individual devices. The environment control stabilizes the temperature of the devices and measures the humidity inside the scanner.

Shifters and PIN Diode The two PIN diodes and the corresponding receiver boards are mounted on the transverse shifter which in turn is placed on the longitudinal shifter. This setup allows to position the PIN diode below any device mounted in the scanning machine. Both shifters are controlled by a dedicated control unit. The two independent shifter positions are set via the first HEBus. The position of the two shifters is measured with an incremental encoder placed on the shifter spindle in steps of 0.04 mm for the transverse and 0.1 mm for the longitudinal shifter. The motors can be driven in a slow or a fast mode. The reproducibility of the positioning of both shifters corresponds approximately to one encoder step which does not affect the measurement of the light output considerably.

Electronic Boards are placed on both sides of the scanning machine. There are two identical boards for each block, i.e. one board drives four modules with a total of 32 LEDs. These boards are able to supply for each module a programmable

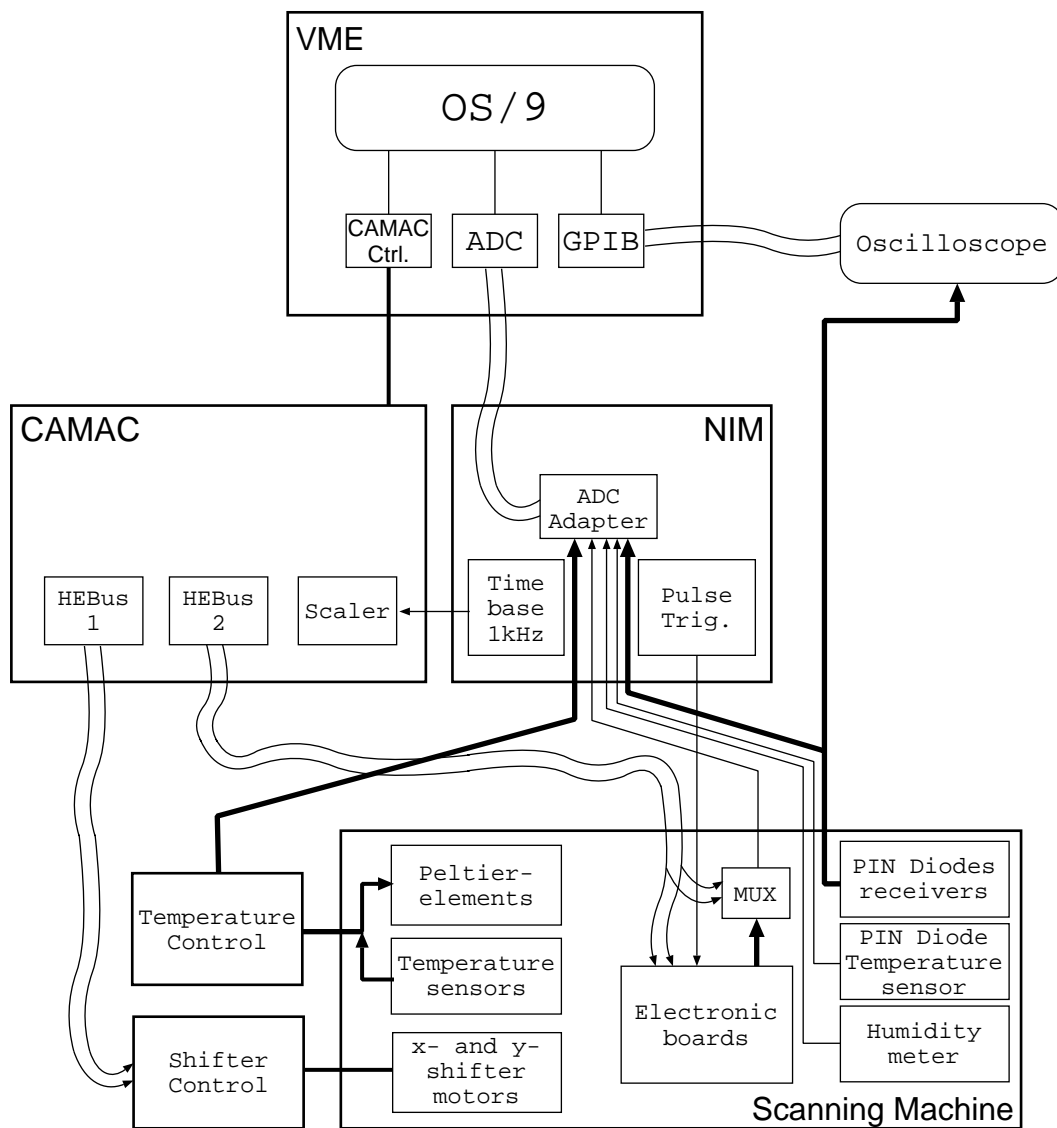


Figure 4.4: Schematic layout of the data acquisition hardware used for the scanning machine

current, and to pulse or to switch on and off individual LEDs. Further, there is a measurement circuit for the LED forward current and the forward voltage. These values are multiplexed into and converted by the ADC. The pulsed mode is controlled by an external NIM pulse and provides current switching times of about 0.7 ns. These pulses are used to measure the fall time and the rise time of the light output. The electronic boards as well as the multiplexer are controlled through the second HEBus.

Environment Control Each block has its own temperature setting and control. The temperature is regulated by Peltier elements and controlled by two individual temperature sensors. The temperature is set manually at the temperature control unit. An additional temperature sensor is placed near the PIN diode in order to measure the temperature of the PIN diode and the adjacent pre-amplifier. The humidity inside the scanner is measured with a humidity meter. All these values are measured with the ADC. The temperature blocks are cooled either by a ventilator or by water, depending on the operating temperature.

4.2.3 Online Software

The software for data acquisition and hardware control was written in C++ in a fully object oriented way and runs on the OS/9 system. A schematic overview of the data and control flow between the different components of the DAQ system is shown in figure 4.5. The main control of all activities is performed by a so called *leddaemon*, which handles the requests from several user interfaces and from the measurement scheduler on one side and the measurement and control program on the other. The *leddaemon* is addressed by a memory resident command handler which assures that only one user at a time is able to have control over the *leddaemon*.

The User Interface The user interface is based on a menu system which gives full control over the measurement process, the hardware configuration and important environment issues. The interface is separated into two parts: the daily used part consisting of data monitoring, measuring and environment checks on one side, and the expert part addressing hardware configurations, software controls and debugging on the other. The latter part is normally hidden from less experienced users.

Measurement and Control The measurement and control algorithms mirror the hardware layout with temperature blocks, ceramic modules and single LEDs. Each of these elements is represented by a C++ class with the corresponding control and measurement functionality. Each class is included in the corresponding parent class, i.e. the class *LED* is included as eightfold array in the parent class *module* which in turn is included as eightfold array in the parent class *block*. All seven *block* classes are joined in the main class *scanner*, corresponding to the whole scanning machine. All functionalities are addressed via a memory resident module, called shared scanner, which feeds the commands recursively through the hierarchical structure. The actual hardware configuration of the scanning machine is stored in a configuration file

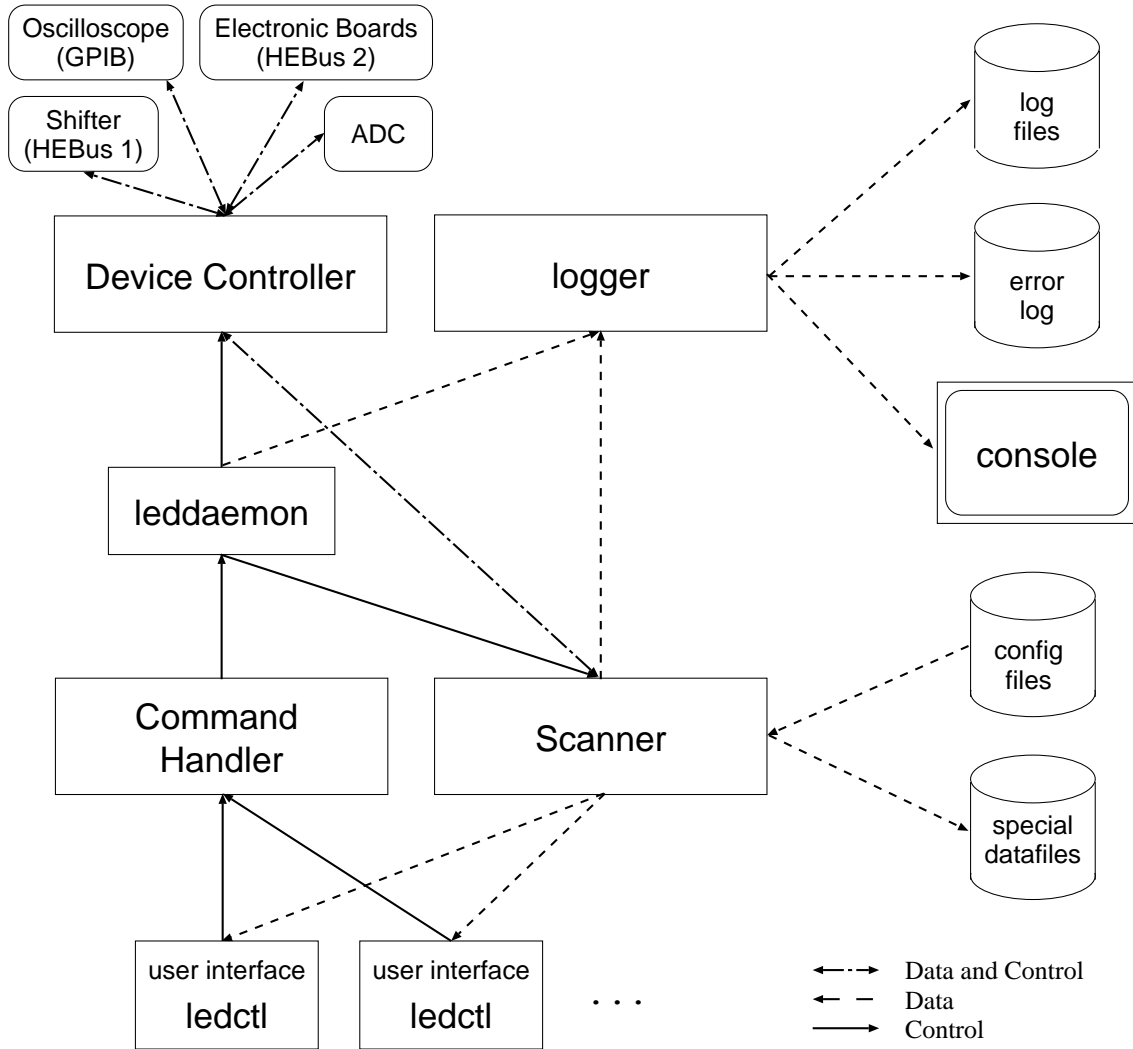


Figure 4.5: Schematic overview of the data and control flow between the different components of the DAQ system

which includes also the last measurement values. This file is read whenever the system is initialized, and it is rewritten after each measurement. Therefore, at all times it represents the actual configuration and can be used to restore the scanner configuration in case of a crash.

Data logging The measurement data acquired and all messages released by the scanning machine are managed by the logger. The logger writes the messages and the data into a log file. This log file is automatically updated whenever new information is available. The messages are displayed on a console in order to give an immediate feedback to the user. Important error messages are also written into a special error file.

Service classes At the lowest level there are several classes handling the real hardware interactions. These classes are mostly split into two sub-classes: an unspecific class concerning basic issues of the hardware used which is now available as a library for further experiments, and a corresponding class which adds the functionalities specific to this particular experimental setup.

4.2.4 Offline Software

The log files generated by the online software on the OS/9 are transferred automatically each hour to a Sun workstation. This machine extracts the measurement data from the automatically generated log files and checks for errors or unexpected measurement values. All error messages are forwarded by e-mail to the user(s) currently responsible for the operation of the scanning machine. The data is filled together with dosimetry information and various normalization values into Ntuples¹. The normalization values (cf. section 4.3.3) are calculated from the measured data and written into conversion databases. Figure 4.6 shows the schematic data flow for the offline processing. The data analysis and display is mainly done with PAW macros.

¹We use the hbook program library, a subroutine package to handle distributions (histograms and data Ntuples) in a Fortran scientific computing environment like the Physics Analysis Workstation (PAW). These programs are all part of the CERN Program Library [39, 40].

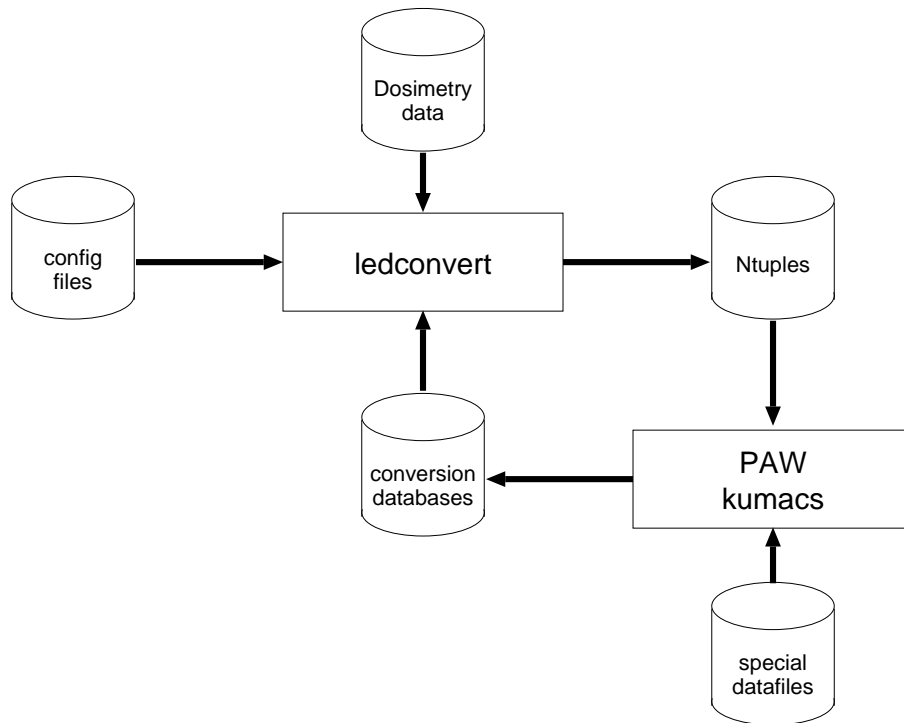


Figure 4.6: Schematic data flow for the offline processing

4.3 Measurement Algorithm

The measurement functionality incorporated into the scanning machine splits into three parts:

Standard measurement of individual devices For each LED/VCSEL the forward current, the forward voltage and the light output can be measured automatically using the 16-bit ADC. Such measurements are performed on a regular basis and can be done for different predefined forward currents. Upon request of the user, additional measurements of the fall and rise time can be made with the oscilloscope.

Special measurements The light output vs. current (L-I) and the voltage vs. current (V-I) curves can be acquired, the lateral light output profile of the device, the so called light cone, can be scanned with the PIN diode and the position of the maximal light output can be determined. These measurements are performed for the pre-irradiation characterization of the devices and later on when necessary.

Environment measurements include the measurement of the temperature of all blocks, the temperature of the PIN diode and the humidity inside the scanning machine. These measurements are made before a standard measurement is initiated and on user request.

4.3.1 The Standard Measurement

For the standard measurement, the forward current, the forward voltage and the light output is measured at the previously determined position of the maximal light output (cf. section 4.3.2.3). Measurements can be done for several predefined forward currents.

The algorithm for this task is optimized to operate the device as short as possible during the measurements. This is important for the first few measurements made after the irradiation, when a fast annealing under forward bias is expected. However, due to the filter used to eliminate the high frequency noise of the PIN diode, it takes a couple of ms until the voltage measured by the ADC reaches its maximal value. Therefore, the measurement of the light output is performed 20 ms after the device is switched on. In order to have a consistent measurement of the forward current and voltage, these measurements are performed after 20 ms, too. Between these measurements, the device is turned off for a few milliseconds in order to measure the bias value. Further, this intermediate time is used to compare the actual measured value with the previous value and to issue a warning if this value differs more than a predefined amount.

In addition to the measurement of the light output, the forward voltage and the forward current with the ADC, the fall and rise time can be acquired by the oscilloscope. During this measurement the LED is switched to the fast current pulse mode for about 30 – 45 seconds. This time is needed for automatically adjusting the measurement range of the oscilloscope, for averaging the waveform and for noise subtraction if necessary. The intrinsic fall time of the measurement system, which includes the current switching time, the response of the PIN diode and amplifier as well as the bandwidth limit of 350 MHz of the oscilloscope, is about 2.1 ns.

For each measurement a data string is written into the log file. The data string contains an identification number and the actual position of the device inside the scanning machine, the accumulated operating time, the temperature of the device, and the actual measured forward current, forward voltage, the light output and the fall and rise time if measured. Additionally, the pre-irradiation values are stored together with the actual values in order to provide a direct comparison.

4.3.2 The Special Measurements

4.3.2.1 I-V and L-I scans

The forward current vs. voltage (I-V) and light output vs. forward current (L-I) scans are initiated on user request. The user can specify the forward current range which will be scanned. As described in section 4.3.1, the measurement of the light output and of the forward voltage is performed 20 ms after the device is switched on. After the measurement at a given forward current, the device is switched off for one second in order to eliminate any effects from thermal heating before the next measurement at the higher current is initiated. The result of these measurements is stored in separate data files, i.e. is not included into the log file.

4.3.2.2 Light Cone Scans

The idea of the light cone scans is to measure the lateral profile of the emitted light, i.e. the light output at a large number of points in a rectangular region around the maximal light output measured. A sample of a light cone scan for a GEC-Marconi LED is shown in figure 4.7.

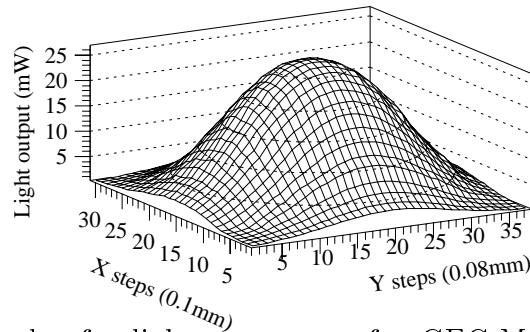


Figure 4.7: Sample of a light cone scan of a GEC-Marconi LED (before irradiation)

4.3.2.3 Position of the Maximal Light Output

In order to determine the position of the maximal light output of a given device, the following strategy is used:

In a first step, both shifters are moved to the position where the maximal light output was seen in the previous search² and the light output is measured. Then both shifters perform alternatively the following procedure: first the transverse shifter moves by ~ 1 mm to one side and measures the light output. If this value is higher than the highest one measured so far, it stays there. Otherwise, this shifter moves the same distance to the opposite side of the starting point and remeasures the light output. If the light output is again lower than the highest one measured so far, the shifter returns to the original position. Otherwise it keeps its position. Then, the longitudinal shifter performs the same procedure and the moving distance is reduced by a factor of two. This is done until the moving distance is below one encoder step of 0.1 mm for the longitudinal shifter and 0.04 mm for the transverse shifter. The new maximum position is compared to the initial one and a new complete maximum search is performed if the distance between these two points is larger than 0.8 mm. This algorithm finds the position of the maximal light output even if it is some millimeters away from the starting point. Of course, there are some checks added in order to prevent an endless loop. For example, the procedure is aborted if there is no light seen at all or if a well defined maximum is not found after three full cycles.

²The initial position of a newly inserted device is calculated from the geometry of the scanning machine. Irradiated devices are inserted at the same position where the pre-irradiation measurements were performed, eliminating the need of a maximum search before the first measurement. The effective position of the maximal light output is determined later on and the first measurements are corrected accordingly.

4.3.3 The Normalization of the Light Output

The light output of LEDs and VCSELs depends on the forward current and the operating temperature. In order to have at any time, independently of the actual operating temperature and forward current, a measure of the light output, the offline software (cf. section 4.2.4) normalizes the light output measured to the default operating conditions of a given device (cf. table 5.2). Thus, the normalized light output of irradiated devices can be directly related to the pre-irradiation measurements made at the default conditions. The resulting relative light output (RLO) is more or less³ independent of higher forward currents (used during the annealing) and of higher temperature (used during the aging).

The dependence of the light output on the forward current is measured before and, if necessary, after the irradiation. This data is fitted with second order polynomial functions and the fit parameters are stored in a conversion database. For the dependence of the forward voltage U_{fwd} on the temperature T only pre-irradiation data acquired at the default current and at different temperatures is used. The light output of LEDs as function of the temperature is fitted with a linear function, whereas for the VCSELs a straightforward temperature correction is not possible (cf. section 5.3.1).

For a better correction of thermal effects in LEDs, the junction temperature of the device is calculated. For this purpose, for about half of the LEDs an individual thermal resistance, i.e. the dependence of the forward voltage from the junction temperature, is determined. This is done by operating the device for five minutes at an elevated forward current of 50 mA for heating the junction up. The power dissipated in the junction is measured by the product of the forward voltage times the forward current. After this heating period, the forward current is lowered to 10 mA. The forward voltage over the still heated junction is measured immediately and after two minutes when the junction temperature has dropped to the value corresponding to the power dissipation at 10 mA. Therefore, the difference between these two forward voltages ΔU_{fwd} corresponds to the difference ΔP in power dissipation at 50 mA and at 10 mA. By using the measured dependence of the forward voltage from temperature, $\partial U_{fwd}/\partial T$, the thermal resistance is derived as

$$R_{thermal} = \frac{1}{\Delta P} \cdot \frac{\Delta U_{fwd}}{\frac{\partial U_{fwd}}{\partial T}} \quad (4.1)$$

The junction temperature can then be calculated as

$$T_{junction} = T_{block} + (R_{thermal} \cdot I_{fwd} \cdot U_{fwd}) \quad (4.2)$$

For those LEDs where no individual measurement of ΔP and ΔU_{fwd} is available, the mean value of the thermal resistance for the corresponding device type is used (cf. table 5.2). The error introduced by this procedure is negligible.

³The deviation of the RLO due to normalization errors is a few percent in the case of the LEDs. Due to the uneven temperature dependence of VCSEL, the normalization does not work well for VCSELs.

4.3.4 Light Output into an Optical Fibre

Due to the fact, that we use unpackaged devices with no fibres attached, we can only measure the light output with the PIN diode inside the scanning machine. In order to obtain a more significant measure of the optical power, a few devices of each kind were operated on a test bench and their light was manually coupled into a 50/125 multi mode fibre by adjusting the fibre with respect to the device until the maximum light output was yielded. The light output at the end of the fibre was measured with a calibrated optical receiver. This value compared to the light output measured in the scanning machine gives a calibration factor for each kind of device. However, this procedure of active alignment is not very representative for packaged devices where the fibre is aligned passively to the LEDs. Comparing our value with the measured light output power of 20 packaged GEC LEDs [14] we found a reduction of light power due to passive alignment of about 20%. Therefore, the calibration factors for all devices given in table 4.1 are reduced by this factor in order to account for the passive alignment.

The large difference in the calibration factors for the ABB Hafo and GEC-Marconi LEDs is mainly due to the different distance of the LED from the PIN diode.

| Calibration Factors | | |
|--|-------------------------------------|--|
| device type | number of manually measured devices | calibration factor ($\mu\text{W}/\text{mV}$) |
| ABB-Hafo LEDs ^a | 5 | 0.024 |
| GEC-Marconi LEDs | 8 | 0.083 |
| VCSELs $I_{th} \simeq 2 \text{ mA}$ | 1 | 0.15 |

^aThe measurement was done with irradiated devices

Table 4.1: Calibration factors used to correlate measurements done with the scanning machine to the light output power coupled to passively aligned 50/125 multi mode fibres

4.4 Irradiation

The devices were irradiated with either neutrons or protons with fluences up to $5 \cdot 10^{14} \text{ n/cm}^2$ and $4 \cdot 10^{14} \text{ p/cm}^2$, respectively. The neutron irradiation took place in the ISIS irradiation facility at the Rutherford Appleton Laboratory (RAL) [41]. The ISIS facility is a spallation neutron source, where protons, which are not trapped by the RF during the acceleration cycle, are stopped by a graphite block backed with copper. The neutron energy spectrum is shown in figure 4.8. The γ/n and the p/n fluence ratios are about 10% and 10^{-3} , respectively [42]. The neutron flux is rather low, varying between $1.5 \cdot 10^{12}$ and $4.3 \cdot 10^{13} \text{ n cm}^{-2} \text{ day}^{-1}$ depending on the operating conditions of the proton synchrotron and the position of the samples. In

| No. of devices | Device type | Fluence (10^{14} n/cm ²) | |
|----------------|----------------------------------|---|----------------|
| | | > 10 keV | < 10 keV |
| 15 | ABB Hafo LEDs | 0.85 ± 0.12 | 26.9 ± 0.5 |
| 23 | ABB Hafo LEDs | 3.2 ± 0.5 | 42.1 ± 0.7 |
| 16 | ABB Hafo LEDs | 5.3 ± 1.8 | 33.9 ± 0.6 |
| 29 | GEC-Marconi LEDs | 0.77 ± 0.12 | 15.3 ± 0.3 |
| 27 | GEC-Marconi LEDs | 4.4 ± 0.5 | 19.2 ± 0.4 |
| 47 | VCSELs ($I_{th} \simeq 2$ mA) | 0.77 ± 0.12 | 15.3 ± 0.3 |
| 31 | VCSELs ($I_{th} \simeq 2$ mA) | 4.4 ± 0.5 | 19.2 ± 0.4 |
| 14 | VCSELs ($I_{th} \lesssim 1$ mA) | 4.4 ± 0.5 | 19.2 ± 0.4 |

Table 4.2: Overview of neutron irradiated LEDs and VCSELs and of the fluences reached. All devices listed in the table were irradiated with ~ 1 MeV neutrons at the RAL ISIS facility, where the dosimetry was done separately for the ~ 1 MeV ($E > 10$ keV) and for the thermal background neutrons ($E < 10$ keV). Since the contribution of thermal neutrons to the displacement damage in GaAs is small compared to the one of ~ 1 MeV neutrons, the thermal neutron fluence was neglected (see text). All devices were not operated during the irradiation.

addition to the ~ 1 MeV neutrons, there is a large background of thermal neutrons which, according to NIEL calculations [17], cause about two orders of magnitude less displacement damage in GaAs than 1 MeV neutrons. For most of the neutron irradiations done at ISIS, the contribution of the thermal neutrons to the total displacement damage is estimated to be less than $\sim 5\%$, and, in the case of the devices irradiated with the most unfavorable ratio of fast to thermal neutrons, less than 10%. Given an uncertainty of the dosimetry of typically 15%, the contribution of the thermal neutron background was neglected.

For the proton irradiation we used the facility provided at the CERN PS in the East Hall. The proton energy is 24 GeV and fluences of approximately 10^{14} p cm⁻² day⁻¹ are available. The protons are extracted from the PS and are therefore delivered in bunches of $\sim 10^{11}$ protons every 14 seconds. Our devices were mounted one behind the other in slide holders aligned to the beam axis. The dosimetry was done with activated aluminum foils, placed in front and at the end of our devices, which were lined up in the slide holder. The major problem was the rather large extent of about 2 cm of our devices in the transverse direction. The beam does cover this area, but it was not always uniform over the whole area. Therefore, the fluence measured in the center of our modules has to be folded with the beam profile measured in front of the devices. This procedure leads specially for the first proton irradiation to rather large uncertainties concerning the individual fluence received by each LED. We addressed this problem later on with more accurate beam profiles and more than one aluminum foil placed not only in the center, but also in the outer part of our devices.

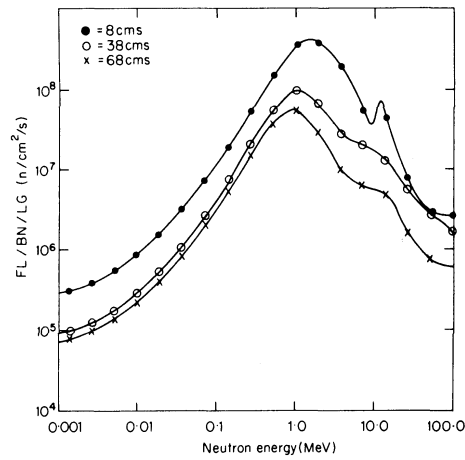


Figure 4.8: Neutron energy spectrum at the RAL ISIS facility, for three different distances from the target [41]

The irradiation of the devices took place at room temperature and no measurements were made during the irradiation. After the irradiation period of typical a few days for the proton irradiation and some weeks for the neutron irradiation, the devices were stored for some weeks in order to reduce their activity.

The neutron irradiated devices were unbiased and open circuited. About half of the proton irradiated devices were operated in a pulsed mode at approximately the default operation current with a duty cycle of 25%. Four ABB Hafo LEDs were operated with 10 mA DC forward current. The rest of the devices was off and unconnected. Tables 4.2 and 4.3 summarize the neutron and proton irradiation conditions and the fluence ranges for the different devices, respectively.

| No. of devices | Device type | Operation mode during irradiation | Fluence (10^{14} p/cm ²) |
|----------------|----------------------------------|-----------------------------------|---|
| 35 | ABB Hafo LEDs | off | $\sim 0.1 - 1.6$ |
| 4 | ABB Hafo LEDs | DC (10 mA) | $\sim 0.7 - 1.3$ |
| 26 | ABB Hafo LEDs | pulsed (10 mA) | $\sim 1.4 - 2.2$ |
| 26 | GEC-Marconi LEDs | pulsed (18 mA) | $\sim 1.7 - 2.6$ |
| 25 | GEC-Marconi LEDs | off | $\sim 1.7 - 2.6$ |
| 7 | GEC-Marconi LEDs | pulsed (20 mA) | $\sim 1.2 - 2.2$ |
| 7 | GEC-Marconi LEDs | off | $\sim 1.2 - 2.2$ |
| 7 | GEC-Marconi LEDs | pulsed (20 mA) | $\sim 2.5 - 4.8$ |
| 7 | GEC-Marconi LEDs | off | $\sim 2.5 - 4.8$ |
| 4 | VCSELs ($I_{th} \simeq 10$ mA) | pulsed (18 mA) | 2.1 ± 0.2 |
| 9 | VCSELs ($I_{th} \simeq 10$ mA) | off | 2.1 ± 0.2 |
| 16 | VCSELs ($I_{th} \lesssim 2$ mA) | off | 2.1 ± 0.2 |
| 19 | VCSELs ($I_{th} \simeq 2$ mA) | pulsed (4 mA) | 1.8 ± 0.2 |
| 17 | VCSELs ($I_{th} \simeq 2$ mA) | off | 1.8 ± 0.2 |
| 15 | VCSELs ($I_{th} \simeq 2$ mA) | pulsed (4 mA) | 3.7 ± 0.3 |
| 15 | VCSELs ($I_{th} \simeq 2$ mA) | off | 3.7 ± 0.3 |
| 3 | VCSELs ($I_{th} \lesssim 1$ mA) | pulsed (2 mA) | 3.7 ± 0.3 |
| 4 | VCSELs ($I_{th} \lesssim 1$ mA) | off | 3.7 ± 0.3 |

Table 4.3: Overview of proton irradiated LEDs and VCSELs, of the operating conditions during the irradiation, and of the fluences reached. All devices listed in the table were irradiated with 24 GeV protons at the CERN PS. The error on the dosimetry is about 10% and is mainly due to uncertainties of the beam profile.

Chapter 5

Devices

5.1 Overview

We used for our test two types of Light Emitting Diodes (LEDs) from ABB Hafo (Sweden) and from GEC-Marconi (U.K.), respectively, and Vertical Cavity Surface Emitting Laser Diodes (VCSELs) from Sandia National Laboratory, Albuquerque (NM, USA). An overview of the devices is given in table 5.1. Except for the different packaging, the ABB Hafo LEDs are identical to those used in the previous life time test [2, 3], where they showed an excellent radiation hardness under neutron irradiation. The GEC-Marconi LEDs are custom devices, which were developed together with a dedicated radiation hard package for possible use at LHC. The kind of VCSELs which we used is still under development and we tested devices from four different production lots. A picture of the different devices mounted on the ceramic boards used in the scanning machine is shown in figure 5.1.

Before any irradiation was done, the devices were installed in the scanning machine (cf. section 4.2) and an initial characterization of the devices was performed. The default measurement conditions and the electrical characteristics of the devices are summarized in table 5.2 and are described in this chapter in more detail.

5.2 Light Emitting Diodes

One possibility for the read-out of the SCT is the use of optical links with radiation hard LEDs as emitters (cf. section 2.4). The light of the LEDs will be coupled to multi mode fibres and transmitted to the off detector receivers. In order to obtain a sufficient S/N even after ten years of operation at LHC, the LEDs will be screened out in order to yield more than $10 \mu\text{W}$ of optical power into a multi mode fibre [8]. However, in the test presented in this work a minimal yield of only $5 \mu\text{W}$ optical power (coupled into a 50/125 multi mode fibre at the default measurement conditions) was required, in order to attain higher statistics with the devices available for testing.

| No. of devices | Description | Manufacturer | Comments |
|----------------|---|---------------------------------------|---------------------------------------|
| 144 | GaAlAs LEDs | ABB Hafo (Sweden) | single device, no longer produced |
| 320 | GaAlAs LEDs | GEC-Marconi (U.K.) | single device, custom manufactured |
| 60 | GaAs/GaAlAs VCSELs $I_{th} \simeq 10$ mA | Sandia National Laboratories (USA) | twenty-fold arrays, in development |
| 440 | GaAs/GaAlAs VCSELs $I_{th} \simeq 2$ mA | Sandia National Laboratories (USA) | twenty-fold arrays, in development |
| 40 | GaAs/GaAlAs VCSELs $I_{th} \lesssim 2$ mA | Sandia National Laboratories (USA) | twenty-fold arrays, in development |
| 60 | GaAs/GaAlAs VCSELs $I_{th} \lesssim 1$ mA | Sandia National Laboratories (USA) | twenty-fold arrays, in development |

Table 5.1: Devices available for the irradiation studies presented in this work. The number of devices stated is the nominal number of devices available, including unconnected VCSELs, devices which were not working initially, and which were not tested due to space constraints in the scanning machine.

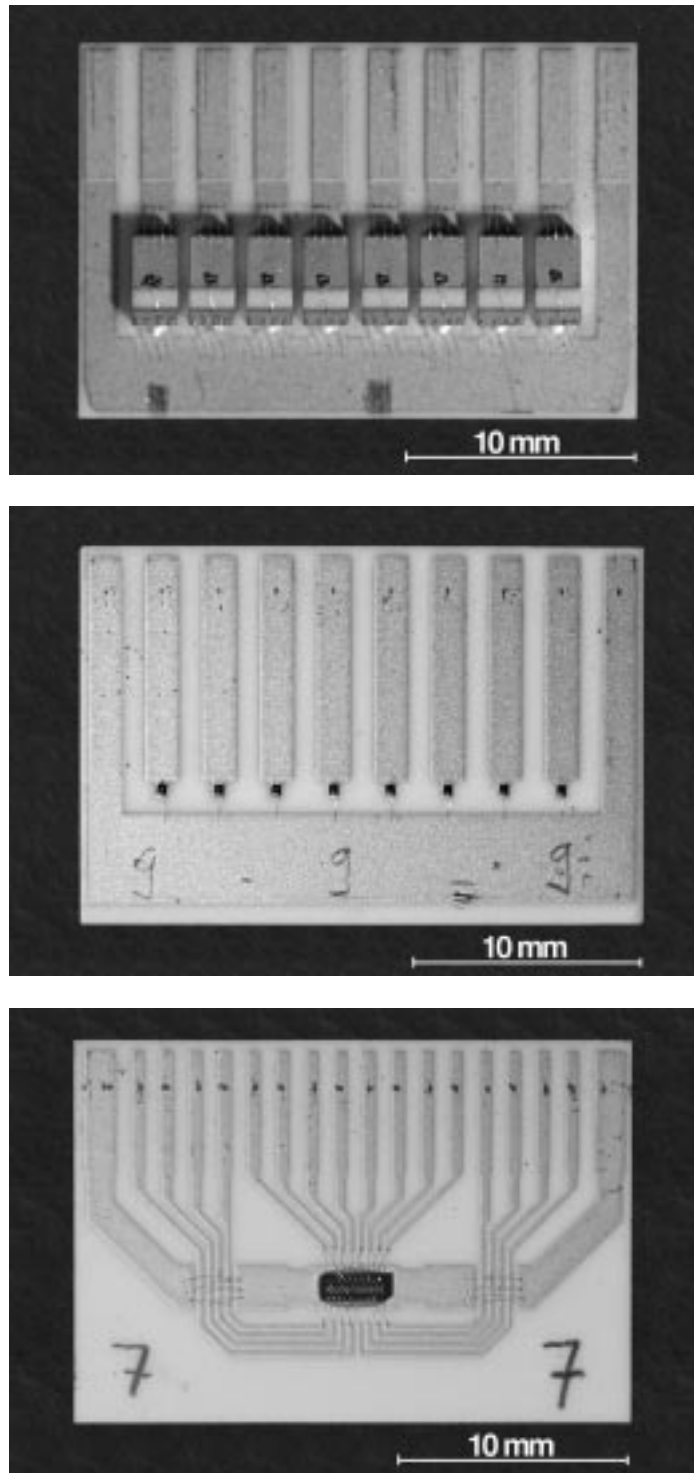


Figure 5.1: Devices mounted onto the ceramic boards used in the scanning machine. Top: eight ABB Hafo LEDs with micro lenses (dark spots); middle: eight GEC LEDs; bottom: one twenty-fold VCSEL array with two times eight connectors.

| | ABB Hafo | GEC- Marconi | VCSEL $I_{th} \approx 10 \text{ mA}$ | VCSEL $I_{th} \approx 2 \text{ mA}$ | VCSEL $I_{th} \approx 2 \text{ mA}$ | VCSEL $I_{th} \approx 1 \text{ mA}$ |
|-------------------------------|--------------|-----------------|---|--|--|--|
| Peak wavelength | 825 | 820 | n/a | 850–860 | n/a | 830–840 |
| Def. temperature | 10 | 10 | 10 | 10 | 10 | 10 |
| Def. forward current | 10 | 20 | 15 | 4 | 3 | 2 |
| Light output | 15 ± 2 | 20 ± 8 | 480 ± 320 | 885 ± 340 | 380 ± 240 | 680 ± 130 |
| Typ. forward voltage | 1.7 | 1.6 | 2.2 | 2.0 | 2.0 | 2.2 |
| Fall time | 1.7 ± 0.2 | 1.2 ± 0.9 | < 1 | < 1 | < 1 | < 1 |
| Rise time | 2.6 ± 0.4 | 3.8 ± 0.6 | < 1 | < 1 | < 1 | < 1 |
| $\partial P_{opt}/\partial T$ | -0.65 ± 0.08 | -1.0 ± 0.2 | n/a | n/a | n/a | n/a |
| Thermal resistance | 57 ± 14 | 57 ± 13 | n/a | n/a | n/a | n/a |

Table 5.2: Electrical characteristics of operational devices at the default operating conditions. The light output is given in terms of optical power that could be coupled into a passively aligned multi mode fibre. The errors stated are RMS errors with no systematic errors accounted for. The quoted fall and rise times are corrected for the intrinsic rise time of 2.1 ns of the measurement system.

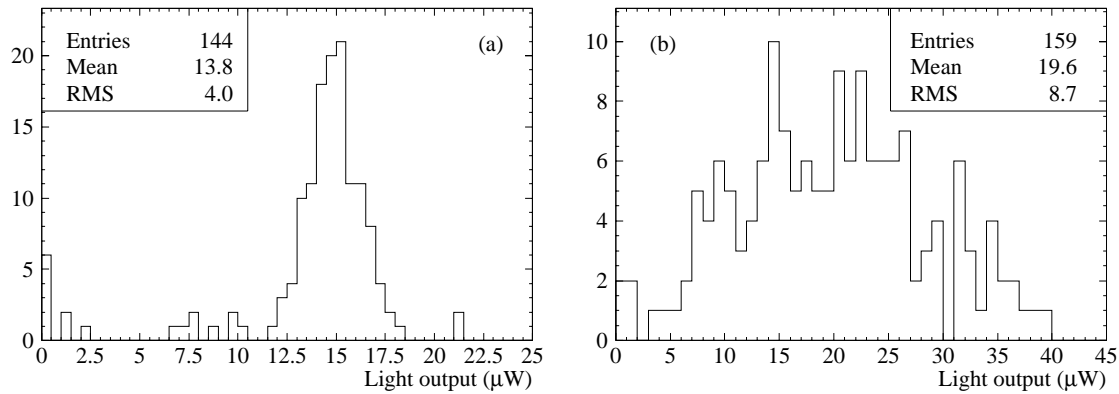


Figure 5.2: Distribution of the light output at $+10^\circ\text{C}$ (a) of the ABB Hafo LEDs at 10 mA forward current and (b) of the GEC-Marconi LEDs at 20 mA forward current.

5.2.1 ABB Hafo LEDs

The ABB Hafo LEDs were chosen initially for possible use in the ATLAS SCT because of their radiation hardness, their outstanding light yield, and their fast response. However, they are not available commercially in a package which is suitable for the application in the SCT. Furthermore, ABB sold the Swedish Hafo to Mitel Corporation [43] and the production of this kind of radiation hard LED type has been stopped [44].

Figure 5.2.a shows the distribution of the pre-irradiation light output at 10 mA and $+10^\circ\text{C}$ of all 144 ABB Hafo LEDs. Due to the fact, that these devices have been tested previously by ABB Hafo, all devices were working. However, 9 out of 144 devices yielded less than $5 \mu\text{W}$ of optical power and were screened out.

5.2.2 GEC-Marconi LEDs

The second type of LEDs tested was developed by GEC-Marconi (U.K.) on behalf of a group at the University of Oxford. These LEDs are specially designed for the use in the SCT and a suitable, radiation hard package is available. However, they have a much higher threshold current than the ABB Hafo LEDs, giving little light at a 10 mA forward current. Therefore, we have chosen a 20 mA forward current as default operating current (cf. table 5.2).

In contrast to the ABB Hafo LEDs, no initial selection was done by the manufacturer, and 17 out of the 176 tested devices gave no light at all. This is mainly due to mechanical defects like broken or not existing bonding wires. The distribution of the light output is shown in figure 5.2.b. The figure shows that another six devices below the $5 \mu\text{W}$ threshold have to be screened out.

5.3 Vertical Cavity Surface Emitting Lasers

Vertical Cavity Surface Emitting Lasers (VCSELs) are an attractive alternative to LEDs as emitters for the optical link. This new type of laser diode has been developed during the last few years. In contrast to older edge emitting lasers, the mirror is grown as paired layers of semiconductor materials into the laser structure itself. Therefore, no mirrors have to be cleaved out of the crystalline structure, making the production and the testing of laser diodes much easier, since the testing is possible already on the wafer. Additionally, due to the fact that the light is emitted perpendicular to the semi-conductor surface, the lasers can be joined to two-dimensional arrays. This is specially important for commercial applications such as optical computer interconnections. Further general informations about VCSELs can be found for example in [45].

Four types of VCSELs from four different production runs have been purchased from Sandia National Laboratories, Albuquerque (NM, USA), in collaboration with the ATLAS group developing the liquid argon calorimeter readout [46]. The lasing threshold current at $+10^{\circ}\text{C}$ is for two types $\sim 2\text{ mA}$ or a bit less, for one type a rather high threshold of $\sim 10\text{ mA}$ was measured, and a few devices have a threshold below 1 mA . Due to the different lasing threshold currents, each VCSEL type was assigned its own default current as listed in table 5.2. The spread of the light output power of the individual devices is large for all four VCSEL types. The fall and rise time of VCSELs within the lasing regime is much faster than those of the electronics used in the scanning machine, hence measurements of VCSEL fall and rise times are not possible with the scanning machine. The thermal behavior of VCSELs depends strongly on the design of the device (cf. section 5.3.1).

In contrast to the more commonly available proton implanted VCSELs, most of the VCSELs in our test are selective oxidized devices [47, 48]. Figure 5.3 shows a sketch of an oxide-confined VCSEL. The oxidized layers are employed to confine the current to a small region of the optical cavity, thus increasing the current density and decreasing the lasing threshold. The oxidized layers have the same purpose as the proton implanted regions in other more commonly used VCSELs. Above and below the optical cavity, distributed Bragg reflector (DBR) mirrors are built from interleaved layers of GaAs and $\text{Al}_x\text{Ga}_{1-x}\text{As}$. The variable x parameterizes the refractive index [49] and ranges from 0.96 in the innermost to 0.16 in the outermost layers [48, 50].

The VCSELs tested were manufactured in a twenty-fold array and mounted onto our ceramic boards. However, in the scanning machine there are only eight electronic channels per module. By adjusting the position of the ceramic modules relative to the connectors, we are able to test 16 of the 20 devices. However, only eight devices can be operated and measured at the same time.

We request for all VCSELs a minimal initial light output of $200\text{ }\mu\text{W}$. This value is much higher than this one used for the LEDs and was chosen in order to exclude devices where the lasing threshold current is very close to the default operating current, since the light output of such devices is very sensitive on forward current and temperature changes.

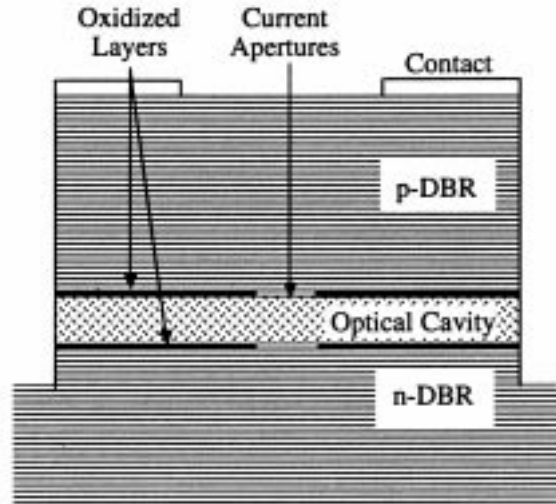


Figure 5.3: Sketch of an oxide-confined VCSEL with distributed Bragg reflectors (DBR) grown above and below the optical cavity. The lateral oxidized layers confine the current to a small region of the cavity [50].

5.3.1 Temperature Dependence of the Lasing Threshold Current

The lasing threshold current of VCSELs is very temperature sensitive, since the threshold current is a function of the alignment of the gain peak and of the Fabry-Perot cavity wave length. This function is not necessarily a monotonic function of the temperature [51], but it has a minimum at the particular temperature where the gain peak and the Fabry-Perot cavity are in resonance. Therefore, VCSELs can be tuned for a desired temperature. A comprehensive review of temperature related effects is given in [52].

The VCSELs used in our test are optimized for room temperature and they show a very uneven behavior at -10°C . However, recent developments lead to laterally oxidized VCSELs with a sub-milliamp threshold current and good light output in a temperature range from 77 K to 370 K [53].

5.3.2 Modal Noise in the Laser Cavity

The VCSEL cavity is tuned for a single mode longitudinal emission. However, in the presence of a reflective external surface like an uncoated optical fibre, the effective cavity length of the laser may be altered. Thus additional longitudinal modes can emerge. This behavior was reported for a feedback strength exceeding 1% [54] and the noise induced may vary by more than 40dB above the level with no feedback [55].

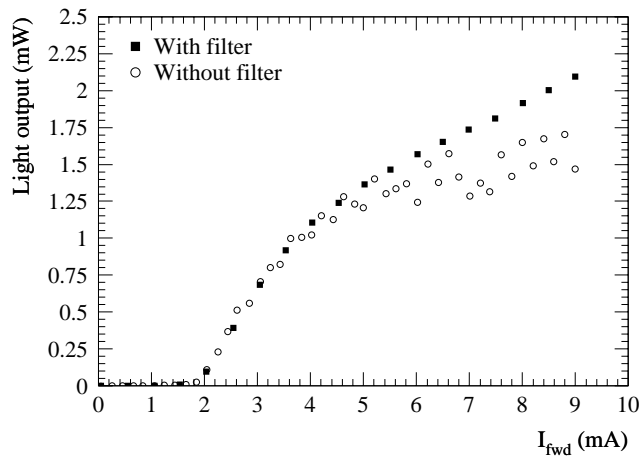


Figure 5.4: L-I curve with and without modal noise from feedback (see text)

We have seen similar effects in the scanning machine. The reflections from the PIN diode back into the VCSEL cavity lead to an increased noise as shown in figure 5.4. Placing a filter with an attenuation of a factor of 8 on the PIN diode improved the signal considerably.

A second well known problem is the mode stability in the transverse direction. Due to the diameter of the active optical cavity in the lateral direction of typical $> 5 \mu\text{m}$, which is large compared to the wavelength of $\sim 0.3 \mu\text{m}$ in the material, transverse electromagnetic (TEM) waves may emerge. However, the reflectivity of the distributed Bragg reflectors decreases with higher TEM modes. Therefore, lower modes are strongly favored [49]. Nevertheless, at higher pump levels, i.e. at higher forward currents for a given device, higher order TEM modes may emerge. Different effects have been discussed in the literature, including spatial hole burning of the lateral gain profile due to thermal lensing [56]–[60] and tuning of the gain peak to the cavity mode [61, 62, 63].

Figure 5.5 shows the light cone of a single VCSEL at different forward currents scanned with the PIN diode at a distance of a few millimeters in front of the VCSEL. The VCSEL emits only at lower forward currents in a single transverse mode and develops higher TEM modes at higher forward currents. The corresponding L-I curve is shown in figure 5.5.a. It shows characteristic bends, when new modes are excited.

The modal noise represents a potential problem when VCSELs are coupled to fibres. One solution is to use a special optical interface like the GUIDECAS^T used in Motorola’s OPTOBUS system [64]. The drawback of such a solution is the price and the possible lack of radiation hardness. However, recent developments lead to a passive self aligned plastic package with a MT connector for a 16-channel two-dimensional VCSEL array [65, 66]. A bit error rate of 10^{-11} was achieved for a 1 Gb/s link. Of course, for application in the SCT, the radiation hardness of the package would need to be tested as well.

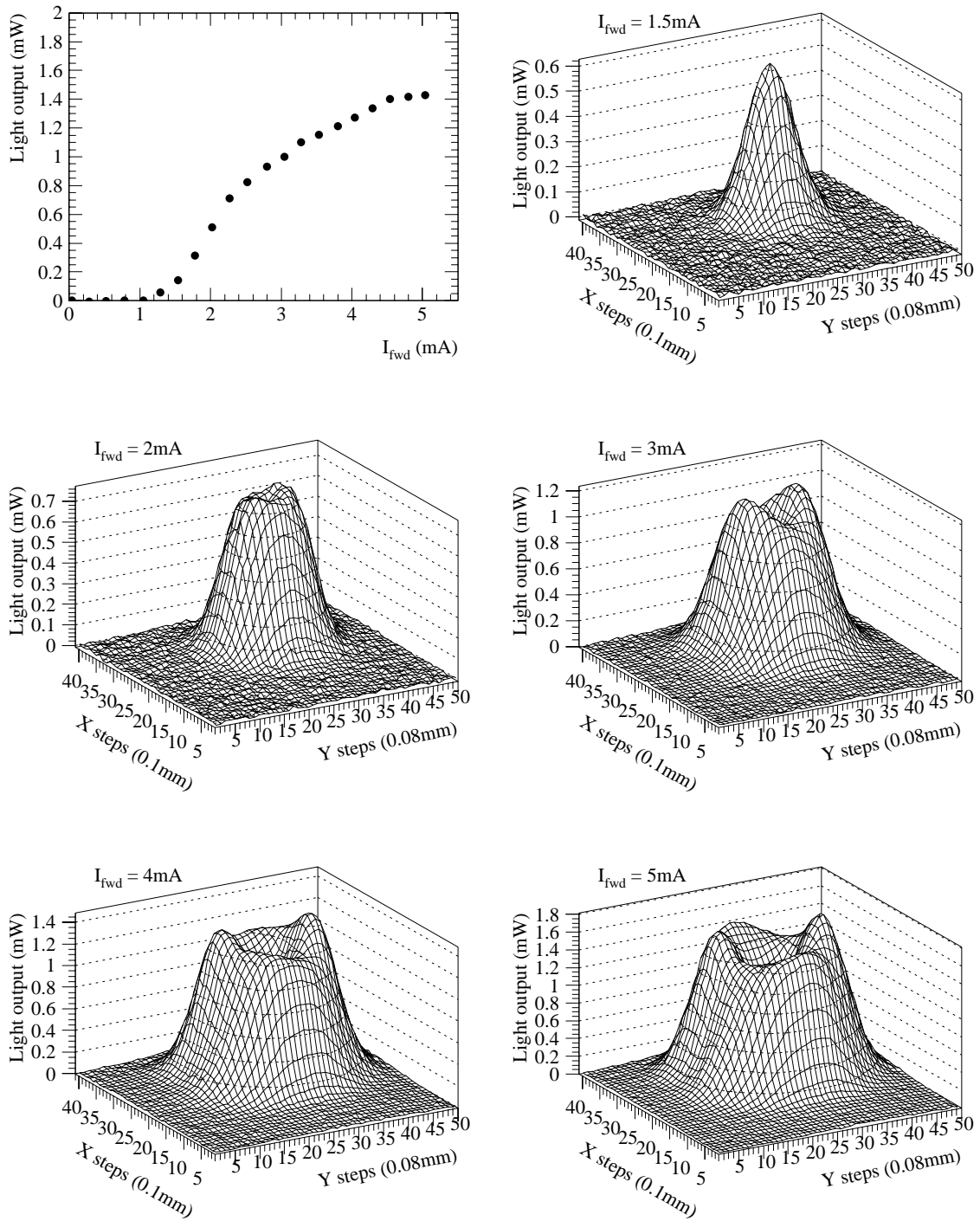


Figure 5.5: Single mode vs. multi mode behavior of VCSELs as a function of the forward current (see text)

Chapter 6

Short Term Results

6.1 Introduction

After the irradiation at ambient temperature at the irradiation facility, the devices were stored (also at ambient temperature) for some days or weeks in order to reduce their activity before shipping them back to the laboratory. After receiving the irradiated devices, they were remounted into the scanning machine and cooled down to either $+10^{\circ}\text{C}$ or -10°C . The first measurement of all devices was done at the default current (cf. table 5.2). In the case of the VCSELs, for some devices L-I and V-I curves were measured, too.

Following the first measurement after irradiation, the forward current was set to the desired annealing current and the devices were operated in DC mode and frequently measured, monitoring the progress of the annealing. The progress of the annealing was inspected regularly. If there was no further annealing observed at a given forward current, the annealing treatment was stopped or continued at a higher current in order to investigate the dependence of the injection annealing on the forward current.

6.2 Damage Constants for GEC-Marconi LEDs

As shown in section 3.2.3, the relative light output after the irradiation before any subsequent annealing treatment is a function of the total fluence ϕ received by a given device (cf. eq. 3.7):

$$\left(\frac{1}{RLO}\right)^{\frac{2}{3}} = 1 + k\phi \quad (6.1)$$

In order to determine the parameter k , it is important that no injection annealing of the primary defects induced by the radiation takes place. Since injection annealing changes the concentration of defect types, the parameter k changes. As long as non linear effects, like e.g. the combination of two defects into a new one are negligible, equation (6.1) will still be valid. However, it might turn out to be very difficult to parameterize the amount of annealing that takes place and thus to determine a meaningful value for k .

Due to the fact, that the GEC-Marconi LEDs exhibit no or only a very slow annealing at the default current of 20 mA, the defect concentration is not altered significantly within the few ms of operating time during the first measurement. Therefore, devices not operated during the irradiation reflect the original radiation induced defect concentrations and can be used for the calculation of the parameters k_n and k_p for neutron- and proton-irradiation, respectively.

Figure 6.1 shows the fit of equation (6.1) for the proton and neutron irradiation. The resulting ratio $k_p/k_n = 3.2 \pm 0.1$ gives a measure of the relative radiation damage induced by 24 GeV protons and ISIS neutrons. This relation is in excellent agreement with the NIEL calculations for GaAs done for 24 GeV protons and ISIS neutrons, where a ratio of 3.2 was found [31]. This result strongly supports the NIEL hypothesis, which is crucial for the extrapolation of radiation hardness studies to the LHC environment.

When a similar fit is done for proton irradiated GEC-Marconi LEDs which were pulsed with a 20 mA forward current during the irradiation, the parameter \tilde{k}_p is lowered to $(6.8 \pm 0.2) \cdot 10^{-14} \text{ cm}^2$. As expected, the resulting damage constant is significantly lower due to the injection annealing already taking place during the irradiation.

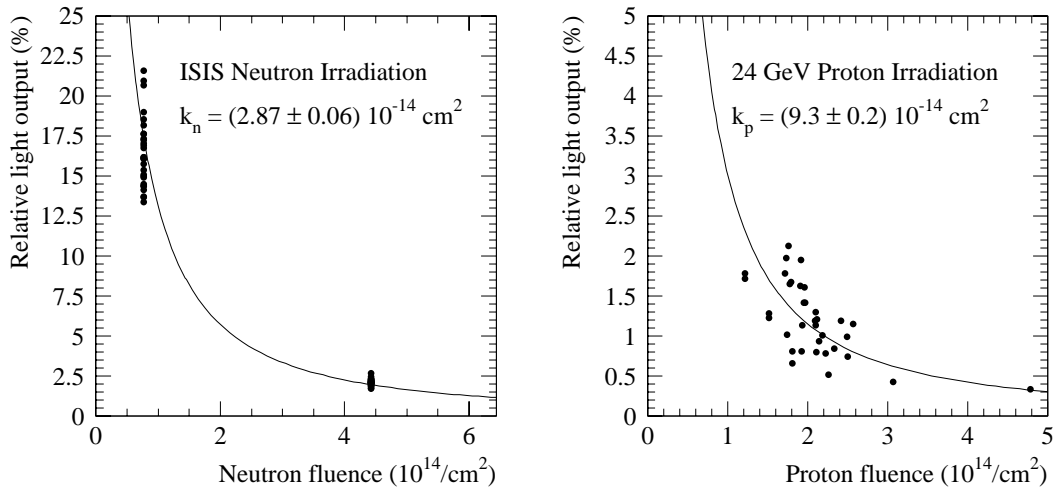


Figure 6.1: Damage function fit for GEC-Marconi LEDs irradiated with ISIS neutrons (left) and 24 GeV protons (right). The errors are the statistical errors of the fitting procedure, assuming an uncertainty of 15% (10%) in the dosimetry of the neutron (proton) irradiation, and an error of 5% for the light output measurements.

6.3 Annealing

As shown in section 4.4 the primary radiation induced defects originate from the displacement of atoms within the semiconductor crystal. Most of these defects recombine within seconds due to thermally activated motion. It is not a priori clear if the thermally activated annealing is the same at room temperature, like in the case of this test, or at the SCT operating temperature of -5°C to -10°C . However, recent irradiation of a few GEC-Marconi LEDs at about -7°C showed no substantial difference in the resulting radiation damage [67].

Defects which are stable at room temperature may be annealed under forward current since the electron-hole recombinations at a defect can increase the defect's mobility. This type of annealing is called injection annealing.

About one third of the devices irradiated were operated in a pulsed mode during the irradiation. Thus part of the injection annealing took place during the irradiation, resulting in a higher light output after the irradiation compared to the devices not operated during the irradiation. This behavior was confirmed by measurements of two ABB Hafo LEDs during the irradiation with $\sim 6 \cdot 10^{14} \text{ p/cm}^2$ showing no significant difference in the final light output compared to the light output after the annealing was finished [68].

In the following, the annealing behavior of the three types of devices in this test will be discussed.

6.3.1 ABB Hafo LEDs

Two typical annealing behaviors of ABB Hafo LEDs are shown in figure 6.2. Figure (a) shows that the light output of an ABB Hafo LED after the irradiation with $1.6 \cdot 10^{14} \text{ p/cm}^2$ was decreased to a few percent. The operation of this device at 10 mA and $+10^{\circ}\text{C}$ for 12 days didn't change the light output significantly. However, when the forward current was increased to 50 mA, a fast annealing occurred. The light output raised to about 40% within a few hours and remained essentially stable.

A different behavior is shown in figure 6.2.b for another ABB Hafo LED irradiated with $3.2 \cdot 10^{14} \text{ n/cm}^2$. The annealing took already place at 10 mA and reached about 60% after a few days of operation at 10°C . However, switching the forward current to 30 mA resulted in an anti-annealing, decreasing the light output to about 40%.

Both annealing and anti-annealing have been observed both after proton and after neutron irradiation. Anti-annealing of ABB Hafo LEDs has been seen at different forward currents between 10 mA – 50 mA, although it is more pronounced at higher currents and not all devices show the same amount of anti-annealing. This anti-annealing and annealing can be understood qualitatively as being due to diffusion processes involving different types of defects in the LED junction. It has been beyond the scope of this work to investigate the microscopic nature of defects, their electrical properties and their concentrations in more detail. Such studies could be performed e.g. using Deep Level Transient Spectroscopy (DLTS) [22, 23].

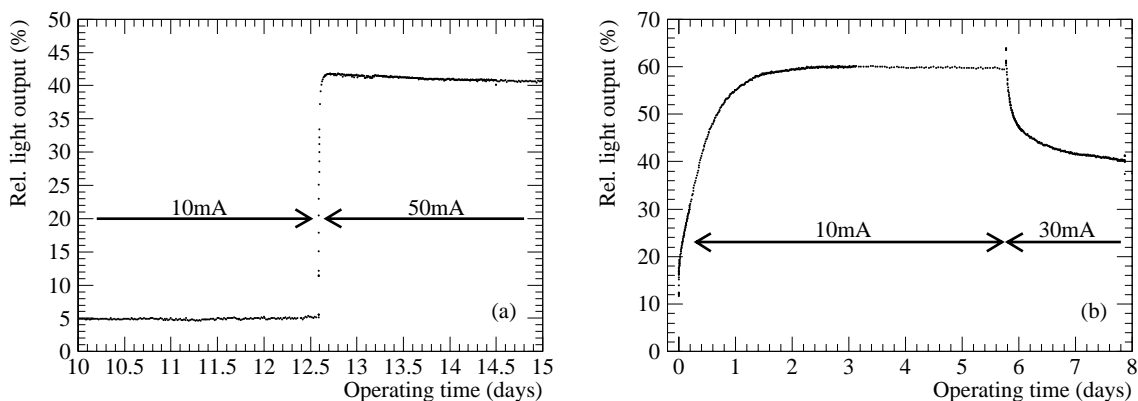


Figure 6.2: Typical annealing of ABB Hafo LEDs: a) Relative light output of an ABB Hafo LED after irradiation with $1.6 \cdot 10^{14} \text{ p/cm}^2$ as a function of operating time. This LED shows very little annealing at 10 mA and $+10^\circ\text{C}$ but a fast annealing at 50 mA. b) Annealing of an ABB Hafo LED after irradiation with $3.2 \cdot 10^{14} \text{ n/cm}^2$ at 10 mA and $+10^\circ\text{C}$ with anti-annealing at a current of 30 mA.

6.3.2 GEC-Marconi LEDs

The annealing behavior of GEC-Marconi LEDs is less favorable than the one of ABB Hafo LEDs. There is almost no or only a very slow annealing at currents below 40 mA (cf. fig. 6.3.a). Therefore, for a significant annealing of GEC-Marconi LEDs an annealing current of 40 mA – 80 mA is necessary. While at a forward current of 40 mA the annealing is still rather slow (cf. fig. 6.3.b), there seems to be no difference in the annealing for currents of 50 mA – 80 mA. Figure 6.3.c shows a GEC-Marconi LED irradiated with $4.4 \cdot 10^{14} \text{ n/cm}^2$ annealing within a few days at 50 mA and -10°C . We also tried to apply higher currents up to 100 mA, but in that case a strong anti-annealing was observed even for unirradiated devices (cf. fig. 6.3.d).

6.3.3 VCSELs

The degradation of VCSELs after the irradiation and the subsequent annealing is best seen in light output vs. current plots as shown in figure 6.4. Both VCSELs have been irradiated with $1.8 \cdot 10^{14} \text{ p/cm}^2$. One was off during the irradiation (figure 6.4.a), the other was operated in pulsed mode with a current of 4 mA and a duty cycle of $\sim 25\%$ (figure 6.4.b). The first measurement after the irradiation (squares) reflects this fact: the un-biased one gives no light up to a forward current of 5 mA while the pulsed device shows very little degradation. After an annealing period of 5.9 day at 4 mA and $+10^\circ\text{C}$ both VCSELs recovered almost completely

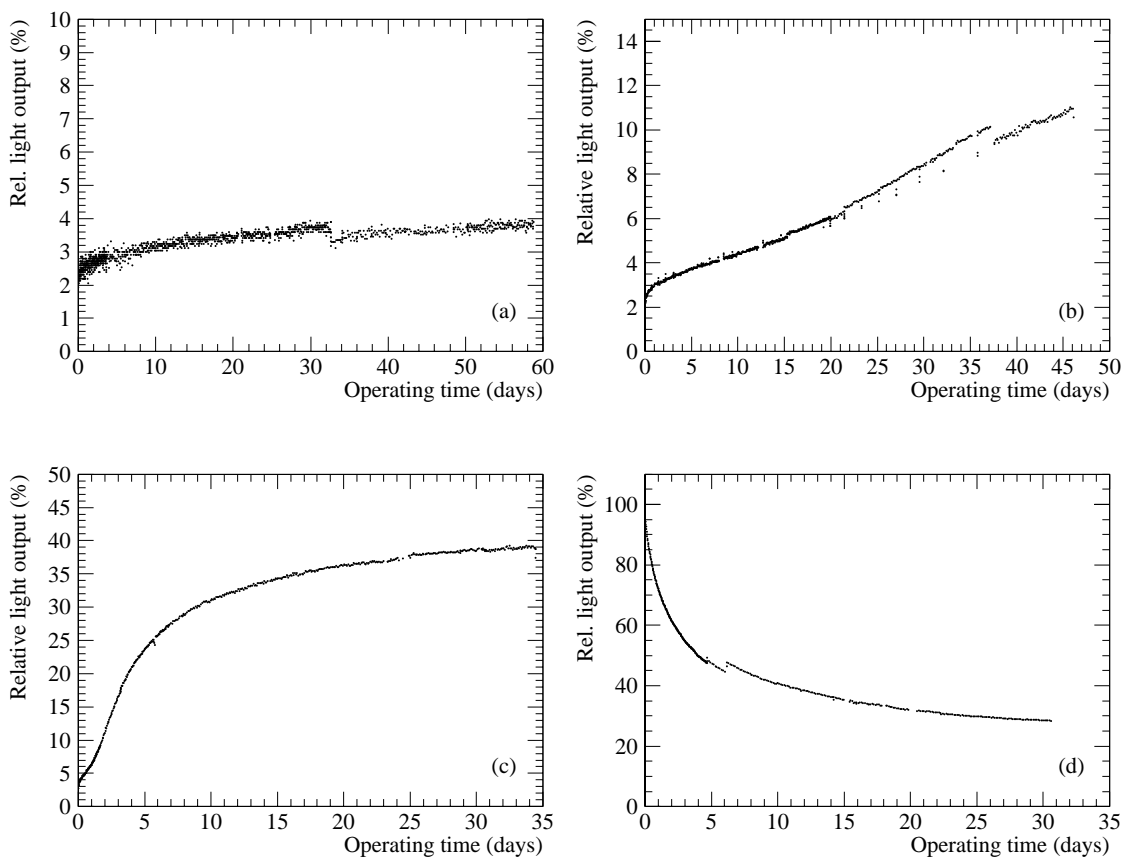


Figure 6.3: Annealing behaviors of GEC-Marconi LEDs: a) A typical LED after $2.1 \cdot 10^{14}$ p/cm² showing very little annealing at 20 mA and 10°C. b) Annealing after $2.2 \cdot 10^{14}$ p/cm² at a forward current of 40 mA and at 10°C. c) Fast annealing after the irradiation with $4.4 \cdot 10^{14}$ n/cm² at 50 mA and -10°C. d) Anti-annealing of an unirradiated LED at a forward current of 100 mA.

6.4 Temperature Dependence of Annealing

The operating temperature for LEDs in the SCT will be between about -5°C and -10°C [8]. In order to investigate the temperature dependence of the annealing, most of the devices were annealed at a temperature of either $+10^{\circ}\text{C}$ or -10°C . The comparison of the annealing behavior of devices irradiated with the same fluence and annealed with the same forward current at either $+10^{\circ}\text{C}$ or -10°C indicates no significant difference in the final relative light output.

However, the annealing of the LEDs was accelerated when the ambient temperature was increased from $+10^{\circ}\text{C}$ to 50°C in order to accelerate the aging. The annealing of most of the ABB Hafo devices was completely finished when the high temperature operation was started. Therefore, only a slight or even no additional annealing was observed at 50°C . The only exception is shown in figure 6.5.a.

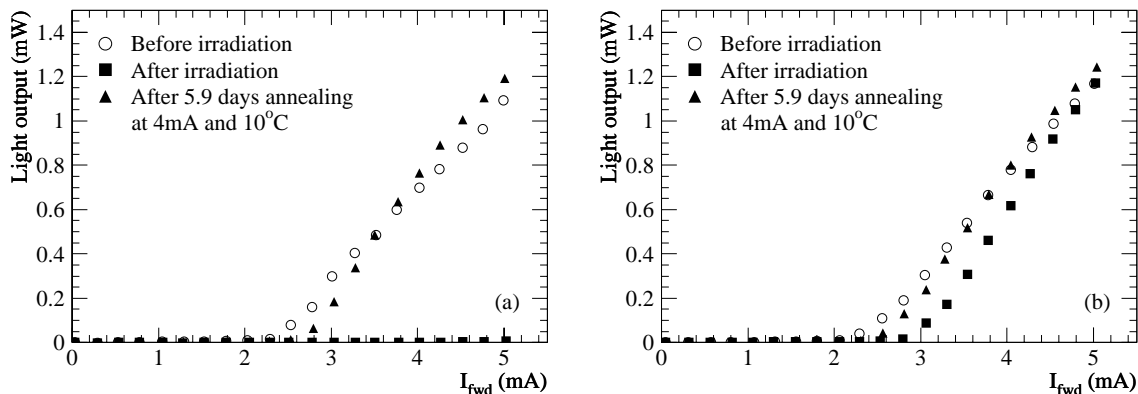


Figure 6.4: Light output vs. current before the irradiation, after the irradiation and after 5.9 days annealing shown for two VCSELs irradiated with $1.8 \cdot 10^{14} \text{ p/cm}^2$: a) VCSEL not operated during irradiation, b) VCSEL pulsed with 4 mA during irradiation

This ABB Hafo LED showed a rather slow annealing after the irradiation with $5.3 \cdot 10^{14} \text{ n/cm}^2$. When the temperature was raised, the annealing was accelerated and reached about 40% of the pre-irradiation value, which is in agreement with the other devices on the same module, which annealed completely before the temperature was increased.

The same behavior was seen by the GEC-Marconi LEDs. Due to the fact, that the annealing of GEC-Marconi LEDs takes much more time, most of the devices did not finish the annealing before the temperature was raised to 50°C . Therefore, the annealing continued during the high temperature operation. Obviously, the amount of annealing observed at 50°C depends on the forward current, too. If the forward current is reduced to the nominal 20 mA, the annealing was mostly stopped (cf. fig. 6.5.b). A few exceptions have been seen like the one shown in figure 6.5.c, exhibiting a very strong annealing at 50°C and 20 mA after 40 days of annealing at 80 mA. In most cases, the aging of the devices was studied at the nominal forward current (cf. table 5.2). However, some of the GEC LEDs which showed still a considerable amount of annealing when the temperature was raised, were further operated at higher forward currents during the aging. These devices continued with an accelerated annealing (cf. fig. 6.5.d). At the time of this writing, the annealing of those devices has not yet finished. Therefore, it is not possible to judge, whether the annealing at higher temperature is just accelerated or if the final relative light output compared to the devices annealed at $\pm 10^\circ\text{C}$ will be higher as well.

6.5 Summary

The short term results are summarized in figure 6.6. The relative light output of the individual LEDs/VCSELs is shown as function of the 24 GeV proton (lower axis) and the ISIS neutron fluence (upper axis), respectively. The two axis are

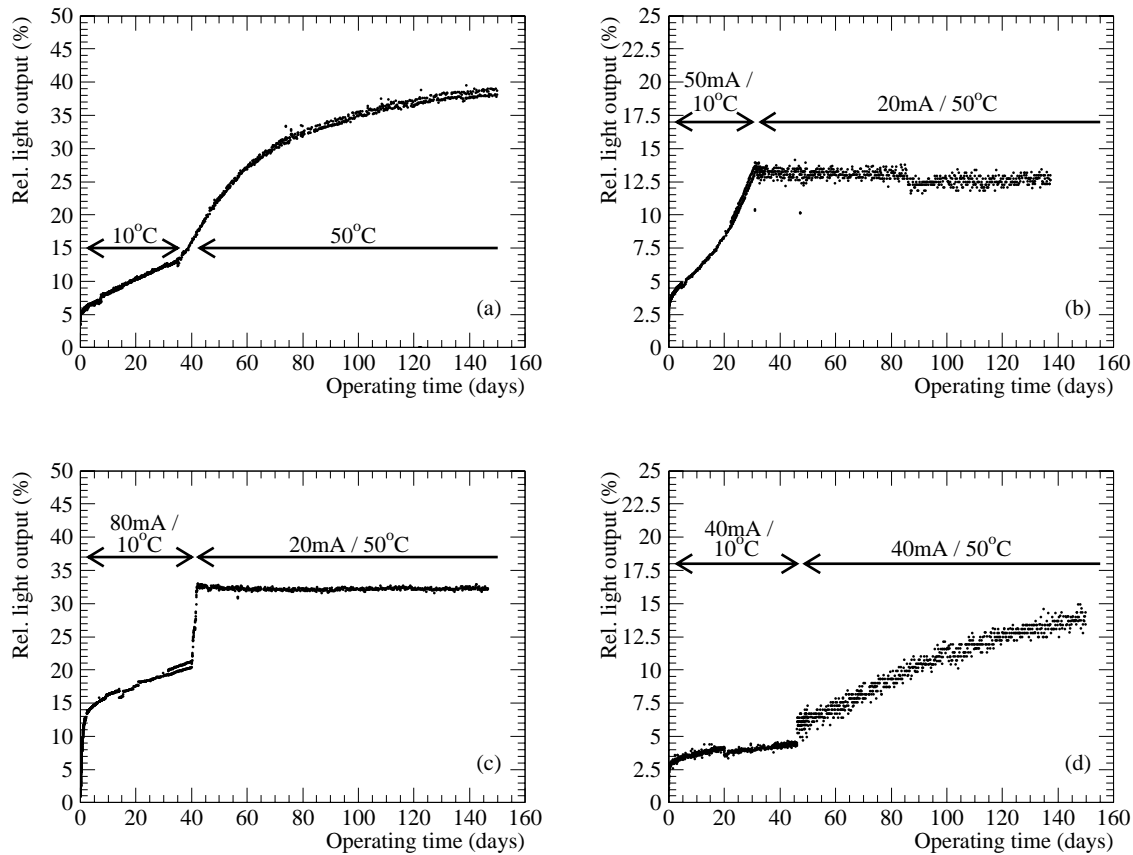


Figure 6.5: Temperature dependence of the annealing: a) this ABB Hafo LED irradiated with $5.3 \cdot 10^{14} \text{ n/cm}^2$ showed an acceleration of the annealing at 20 mA when the temperature was raised; b) most of the GEC-Marconi LEDs stopped the annealing when the forward current was decreased to 20 mA; c) one example of a GEC-Marconi LED annealing quickly at elevated temperature but low forward current; d) the annealing of this GEC-Marconi LED at a forward current of 40 mA accelerated when the temperature was increased.

scaled such that the NIEL (cf. section 3.2.2) calculated for GaAs in [31] is the same for corresponding fluences. Therefore, if the relative light output of LEDs after irradiation depends on the NIEL, there should be no difference between neutron and proton irradiated devices. Despite the large spread of our data, which is partly due to large uncertainties in the dosimetry, the neutron and proton data agrees fairly well.

The importance of injection annealing is evident when comparing the little dots with the larger symbols in figure 6.6. The former denote the first measurement made after the irradiation, the latter the relative light output after an annealing period of up to several weeks at the maximum forward current indicated in the legend. In most (but not all) cases no signs of further annealing were observed (cf. section 6.4).

A comparison of the ABB Hafo LEDs annealed with a maximum current of 30 mA (full circles) with those annealed at up to 50 mA (hollow circles), shows that for the latter the final relative light output is higher. Thus, the degree of annealing depends on the maximum annealing current applied.

The outstanding radiation hardness of VCSELs is seen in this plot, too. VCSELs irradiated with fluences up to $3.7 \cdot 10^{14}$ p/cm² yield after a short annealing period of a few hours to days as much light as before the irradiation. Some devices have an even higher light output as before. We suppose that this is due to a burn-in effect. Unfortunately, we have not been able to perform a burn-in prior to the irradiation due to the late arrival of most of the VCSELs which left only a few days between the reception of the devices and the irradiation period.

6.6 Behavior of Failing Devices

After the irradiation or during the annealing period 6 LEDs and 8 VCSELs died or did not show any annealing. Further, 11 GEC LEDs irradiated with a fluence between $3.0 \cdot 10^{14}$ p/cm² and $4.8 \cdot 10^{14}$ p/cm² are annealing very slowly and have to be considered as dead, too. There is a variety of failure characteristics as summarized in figure 6.7 and in table 7.2:

- The LED behaves no longer as a diode but as an ohmic resistor. This is the case for one ABB Hafo LED after $0.7 \cdot 10^{14}$ p/cm² and one GEC-Marconi LED after $2.2 \cdot 10^{14}$ p/cm² (shown in figure 6.7.a). The latter one gave some light after the irradiation, but died within about 30 min of operation as shown in figure 6.7.b.
- The light output of the device is very low and no significant annealing at a given forward current is observed, in contrast to the remaining devices on that particular module. One ABB Hafo LED after $5.3 \cdot 10^{14}$ n/cm² under a forward current of 10 mA (shown in figure 6.7.c) and one GEC-Marconi LED after $2.3 \cdot 10^{14}$ p/cm² under a forward current of 40 mA fall into this category. However, the GEC-Marconi LED was very weak already before the irradiation, yielding less light than the $5 \mu\text{W}$ required for inclusion into the overall statistics.

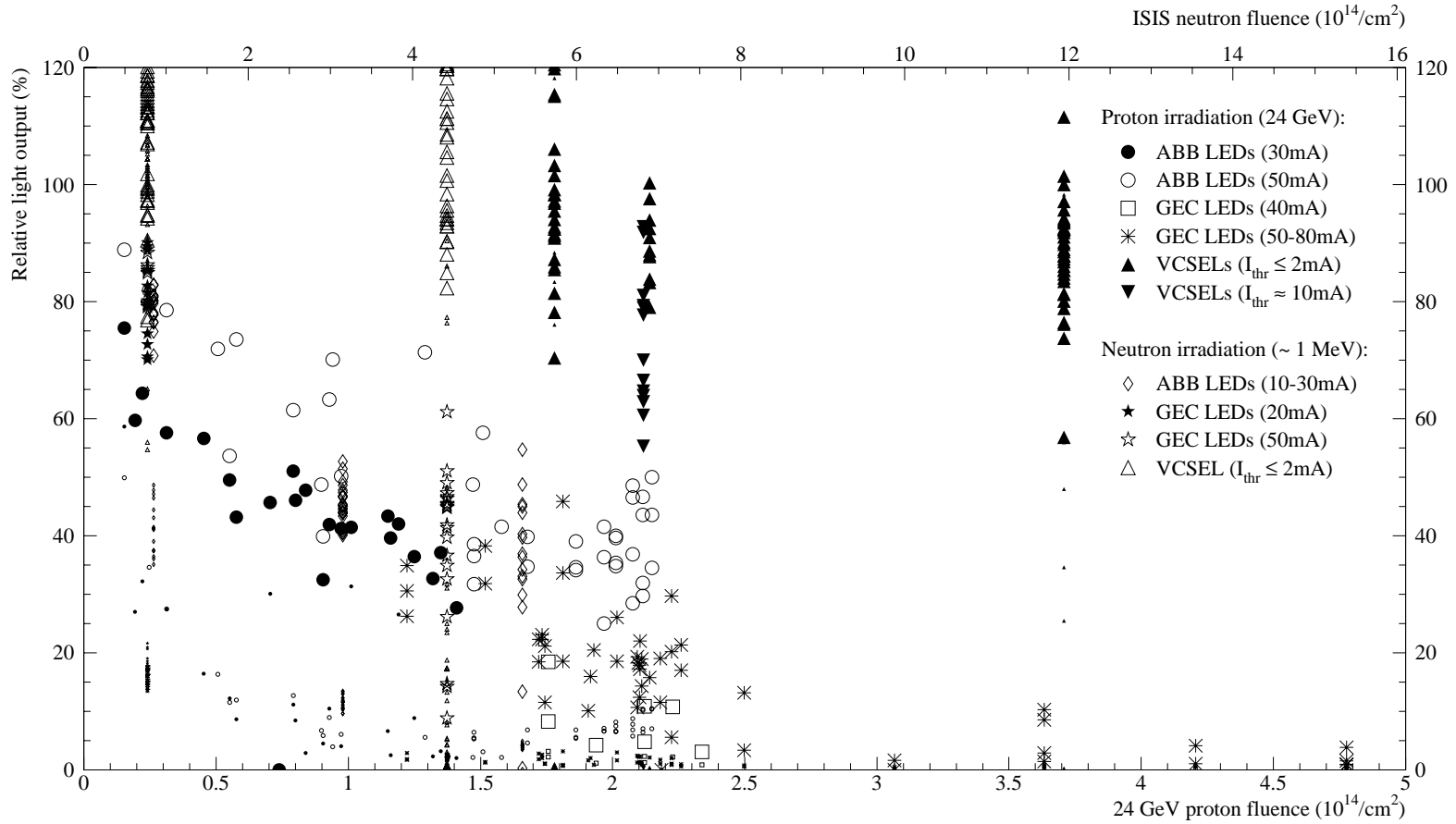


Figure 6.6: Relative light output of individual LEDs and VCSELs after the irradiation as a function of fluence. The little dots denote the first measurement made after the irradiation. The larger symbols show the relative light output after an annealing period of up to several weeks at the maximum forward current indicated in the legend. In most (but not all) cases no signs of further annealing were observed. The VCSELs have been annealed at the default current at $\pm 10^\circ\text{C}$. Both proton and neutron irradiation data is shown and scaled according to the NIEL in GaAs (cf. section 3.2.2).

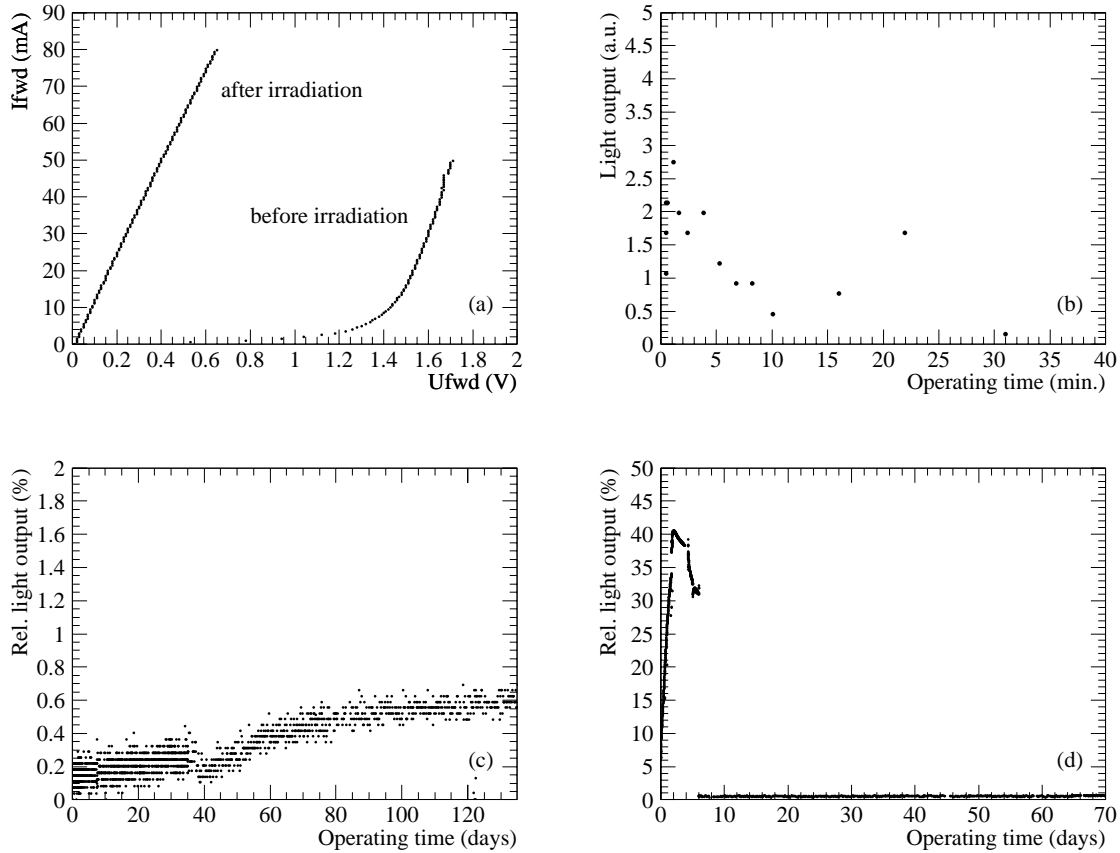


Figure 6.7: Some examples of failing LEDs: a) this GEC-Marconi LED behaves after the irradiation with $2.2 \cdot 10^{14}$ p/cm² no longer as a diode but as an ohmic resistor; b) a GEC-Marconi LED dying within the first minutes of annealing after irradiation with $2.2 \cdot 10^{14}$ p/cm²; c) no significant annealing is seen for this ABB Hafo LED after $5.3 \cdot 10^{14}$ n/cm² under a forward current of 10 mA; d) another ABB Hafo LED showed annealing and anti-annealing after the irradiation with $2.1 \cdot 10^{14}$ p/cm², but yielded almost no light after a storage period of three months at room temperature.

- The LED anneals after the irradiation, but after a storage period of three months at room temperature, the light output falls back to a few percent. This behavior has been observed for two ABB Hafo LEDs after $2.1 \cdot 10^{14}$ p/cm² (shown in figure 6.7.d) and $4 \cdot 10^{14}$ p/cm² respectively. However, the latter LED is excluded from the failure statistics, because the light output of 1 μ W before the irradiation was too low.
- The VCSEL does not yield any light after the irradiation, but the electrical characteristics are inconspicuous. This is the case for two VCSELs, one with a lasing threshold of $\simeq 2$ mA after the irradiation with $1.8 \cdot 10^{14}$ p/cm² and one with a threshold of $\lesssim 1$ mA after the irradiation with $4.4 \cdot 10^{14}$ n/cm².
- The light output after the irradiation is comparable to the other devices irradiated with the same fluence, but the VCSEL dies within seconds when operated. This behavior was seen by three VCSELs with a lasing threshold of $\lesssim 1$ mA after the irradiation with $4.4 \cdot 10^{14}$ n/cm².
- There is no light output after the irradiation and the forward voltage is very low. This is the case for two VCSELs with a lasing threshold of $\lesssim 1$ mA after the irradiation with $4.4 \cdot 10^{14}$ n/cm².

A detailed statistics of all devices irradiated with fluences anticipated for ten years of LHC operating is given in section 7.3.

Chapter 7

Long Term Results

7.1 Introduction

In order to make any prediction on the long term reliability of the irradiated LEDs and VCSELs, the aging has to be accelerated. Therefore, the operating temperature of the devices was increased to 50°C once the annealing was finished or any further annealing would have taken an unreasonably long time. The devices were then operated at the default current for several months. At the time of this writing, the high temperature operating time achieved corresponds to an operating time of up to 40 years in the ATLAS SCT.

7.2 The Acceleration of Aging

In order to make any prediction on device life time in a reasonable amount of time, the aging of the devices studied has to be accelerated. We used two considerations for this purpose:

- It is generally believed that aging of LEDs takes place only under forward bias. Thus we can achieve an acceleration factor of 12 with respect to the LHC by operating the devices with a DC current. This factor is based on the estimate, that a) the LHC will run about 100 days per year, b) the average link occupancy is about 50%, c) the LEDs are off when no data is transmitted, and d) the 0 and 1 bits are balanced.
- An additional acceleration factor is obtained by increasing the temperature. The dependence of the mean LED lifetime τ is given by [69, 70, 71]:

$$\tau \propto \exp \frac{E_a}{kT_j} \quad (7.1)$$

where T_j denotes the junction temperature and E_a the thermal activation energy. The latter depends on the composition and the fabrication of the LEDs and must be determined experimentally. For both types of LEDs E_a is not known. Therefore, we are not able to calculate the acceleration factor

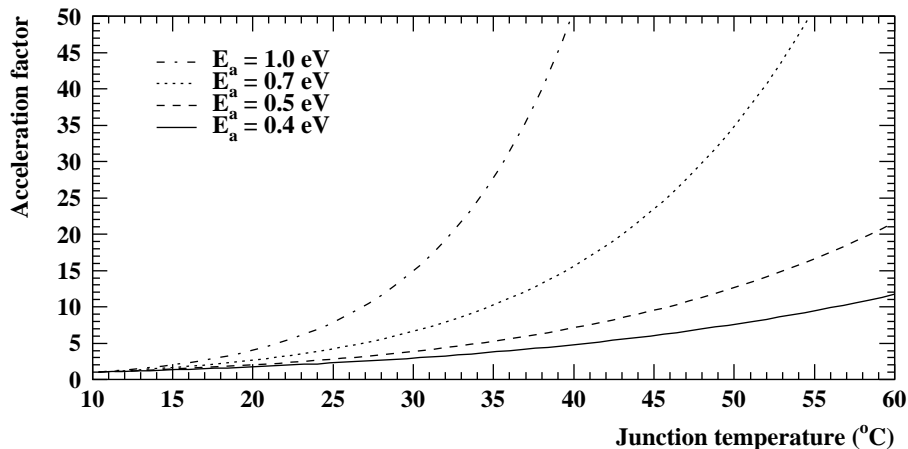


Figure 7.1: Acceleration factors for different thermal activation energies E_a , calculated with respect to aging at $T_j = +10^\circ\text{C}$

with precision. However, typical values found in the literature for E_a are in the range from 0.4 to 1.0 eV. Figure 7.1 shows the acceleration gained by raising the temperature with respect to aging at a nominal operating temperature of $+10^\circ\text{C}$ ¹ for some values of E_a . As a conservative estimate, we use an acceleration factor of 10 for the aging at 50°C . Any additional acceleration due to higher forward currents during the annealing is not taken into account.

The acceleration of the aging for the VCSELs depends on the operating mode of the optical link. It is not yet clear, if the VCSELs can be switched on and off during the data transmission as will be the case for the LEDs. Probably there will be a constant current holding the VCSEL near or above the threshold current when no data is transferred. Therefore, only a factor of three could be gained by operating the devices in DC mode compared to the operation in the SCT, which will run only about 100 days per year.

The dependence of the VCSEL life time from temperature does follow the same relation as those for LEDs stated in equation (7.1) [48]. However, the activation energy E_a for VCSELs is not known. Therefore, no acceleration factor due to the operation of VCSELs at higher temperatures can be stated at present.

7.3 Life Time of Irradiated LEDs and VCSELs

In order to test the life time of the irradiated devices, they were operated at an elevated temperature of 50°C for several months. As shown in section 7.2, this procedure accelerates the aging of LEDs by a factor 120 with respect to the operation in the SCT.

¹The operating temperature in ATLAS SCT will be between -5°C and -10°C resulting in an additional acceleration factor compared to $+10^\circ\text{C}$ which is not taken into account.

Table 7.1 shows the operating time obtained so far and the estimated equivalent operating time in the SCT for the different devices. All devices used for the statistics have been irradiated with a minimum fluence of $2 \cdot 10^{14}$ n/cm² or $0.6 \cdot 10^{14}$ p/cm², where the proton fluence given corresponds to the neutron fluence if the radiation damage scales accordingly to the NIEL hypothesis (cf. section 3.2.2). The fluence used for the statistics is approximately twice as high as the maximum fluence expected in the SCT during ten years of LHC operation, and about twice as high as what the detectors can withstand. This assures that the optical link will be operational at least as long as the detectors, ensuring that the less expensive optical link does not limit the operating time of the expensive electronics and detectors in the SCT.

Devices yielding less than 10% relative light output after the annealing treatment and after the aging are considered as dead. This number is much lower than the 50% used as standard definition in industry. It is deduced from the S/N requirement of the optical link proposed in the SCT. In the case of the SCT, LEDs with a light output of less than $10 \mu\text{W}$ coupled into a multi mode fibre are screened out. Therefore, the weakest LED will still yield an optical power of $1 \mu\text{W}$ after ten years of operation in the SCT. This corresponds to a S/N of 33^2 , which is considered to be sufficient for a read-out link with a bit error rate below 10^{-9} .

As mentioned in section 5.2, we used all LEDs yielding more than $5 \mu\text{W}$ into a multi mode fibre. The lower value was chosen to attain higher statistics. There is no indication that the additional LEDs yielding a light output of $5 - 10 \mu\text{W}$ behave different from the brighter devices. In order to use the same criteria, VCSELs yielding less than 10% of the initial light output are considered as dead, too. However, a VCSEL with 10% of the initial light output will still yield more light than a bright LED before the irradiation.

As shown in section 6.3.2, the annealing current for the GEC LEDs must be in the range of $40 - 80$ mA in order to have a considerable annealing after the irradiation. Therefore, GEC LEDs with a maximum annealing current below or above this range are excluded from the statistics.

No devices failed during the high temperature operation. However, some devices failed right after the irradiation or during the annealing. The behavior of failing devices is discussed in section 6.6, and a summary of all dead devices is given in table 7.2.

Three out of 91 ABB Hafo LEDs have failed. Two were dead right after the irradiation, one showing an ohmic behavior and one giving very little light with virtually no annealing at 10 mA. The third device annealed after the irradiation, but died after a three months storage period.

Three failures out of 58 GEC-Marconi LEDs irradiated with a maximum fluence of $2.5 \cdot 10^{14}$ p/cm² have been found. All three devices were dead right after the irradiation or died within a few minutes. After the irradiation with even higher

²This number is based on measurements with a prototype optical link using GEC-Marconi LEDs and scaled to the ATLAS system, giving an initial S/N of 363 [8]. Beside the degradation of the LEDs an additional factor 0.9 is taken into account for the attenuation in the irradiated optical fibre.

| Device | Particle | Fluence ($10^{14}/\text{cm}^2$) | Irrad. devices | Failing devices | DC operating $\pm 10^\circ\text{C}$ | Operating time (days) 50°C | Corresponding time in the SCT (years) |
|---|----------|--------------------------------------|-------------------|--------------------|--|---|--|
| ABB Hafo LEDs | n | 3.2 / 5.3 | 39 | 1 | 1 ... 35 | 130 ... 133 | ~ 44 |
| | p | 0.6 ... 2.2 | 52 | 2 | 6 ... 44 | 59 ... 133 | 20 ... 45 |
| GEC-Marconi LEDs | n | 4.4 | 12 | 0 | 15 ... 18 | 40 | ~ 13 |
| | | | 7 | 0 | 34 | 0 | ~ 1 |
| | p | 1.2 ... 2.5 | 30 | 1 | 18 ... 40 | 39 ... 114 | 13 ... 39 |
| | | | 9 | 2 | 40 ... 70 | 0 | ~ 2 |
| VCSELs ($I_{th} \approx 10\text{ mA}$) | p | 3.0 ... 4.8 | 6 | 5 | 18 | 39 | ~ 13 |
| | | | 6 | 6 | 70 | 0 | ~ 2.3 |
| | n | ~ 2.1 | 7 | 0 | 5.4 | 59 | |
| | | | 6 | 0 | 2.4 | 0 | |
| VCSELs ($I_{th} \approx 2\text{ mA}$) | n | ~ 4.4 | 15 | 0 | 4.3 / 6.2 | 7.3 | |
| | | | 16 | 0 | 5.0 | 0 | |
| | | | 17 | 1 | 4.8 ... 9.1 | 4.4 ... 64 | |
| | p | ~ 1.8 | 19 | 0 | 6.7 ... 9.1 | 0 | |
| | | | 15 | 0 | 4.9 / 9.1 | 64 | |
| | | | 15 | 0 | 7.6 / 9.1 | 0 | |
| VCSELs ($I_{th} \lesssim 2\text{ mA}$) | p | ~ 2.1 | 8 | 0 | 2.2 | 122 | |
| | | | 8 | 0 | 5.2 | 0 | |
| | | | 8 | 3 | 4.5 | 7.3 | |
| VCSELs ($I_{th} \lesssim 1\text{ mA}$) | n | ~ 4.4 | 6 | 3 | 5.0 | 0 | |
| | | | 5 | 0 | 5.0 | 64 | |
| | | | 2 | 0 | 2.9 | 0 | |

Table 7.1: Current statistics of life time studies. GEC-Marconi LEDs with an annealing current below 50 mA or above 80 mA as well as devices irradiated with less than $2 \cdot 10^{14}$ n/cm² or $0.6 \cdot 10^{14}$ p/cm² are not included. Failing devices yield less than 10% of the initial light output after the annealing treatment and the aging.

Acceleration factors for VCSELs depend on the operating mode of the optical link.

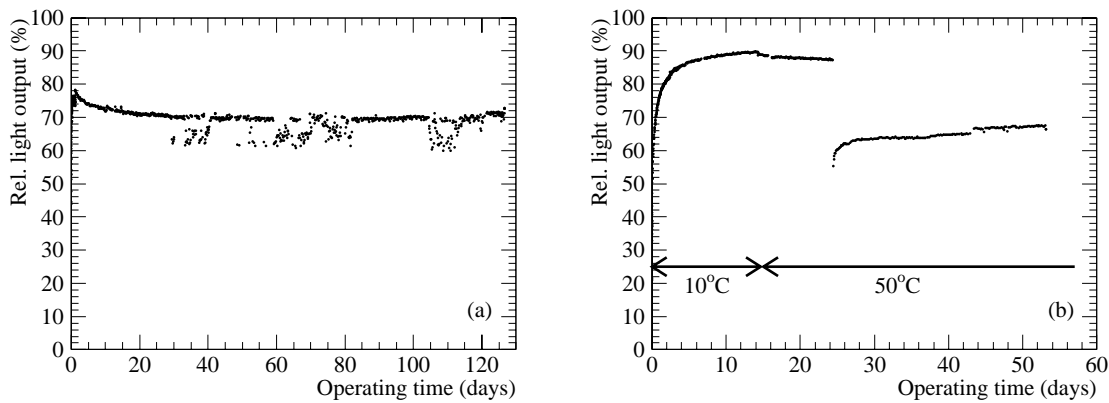


Figure 7.2: The long term stability of two LEDs: a) this ABB Hafo LED irradiated with $0.85 \cdot 10^{14}$ n/cm² shows some anti-annealing and instabilities; b) this GEC LED irradiated with $0.77 \cdot 10^{14}$ n/cm² exhibits an unexplained drop in the light output during the high temperature operation.

fluences, the GEC LEDs yielded nearly no light and showed no or only a very slow annealing at 50 mA. Only one out of 12 devices has reached a relative light output above 10% after an annealing period of up to 70 days.

The VCSELs with a threshold current of about 2 mA seem to be very radiation hard. Only one out of 113 devices irradiated with fluences up to $3.7 \cdot 10^{14}$ p/cm² has failed. The same seems true for the VCSELs with a threshold current of 10 mA. There are no failures out of 13 devices irradiated with $2.1 \cdot 10^{14}$ p/cm². However, the VCSELs with a threshold current below 1 mA have shown six failures in a total of 21 devices irradiated with $3.7 \cdot 10^{14}$ p/cm² or $4.4 \cdot 10^{14}$ n/cm². Although the statistics is low, it seems that this type of VCSEL is less radiation hard than the devices with a higher threshold current.

7.4 Long Term Stability

The light output of most of the devices operated at 50°C and at their default current remained essentially stable. However, some devices exhibited a slow anti-annealing of a few percent per month during the high temperature operation, and some ABB Hafo LEDs showed instabilities of the light output. An example of an ABB Hafo LED showing both behaviors after the irradiation with $0.85 \cdot 10^{14}$ n/cm² is presented in figure 7.2.a.

Figure 7.2.b shows a GEC LED irradiated with $0.77 \cdot 10^{14}$ n/cm² exhibiting a sharp drop in the light output during the high temperature operation. This is up to now the only LED showing a dramatic drop during the aging. This LED belongs to the three brightest GEC LEDs in our test, yielding 38 μW of optical power before the irradiation. Beside this fact, we do not have any clue what might be the cause for this drop. Even after the drop, the light output would be sufficient for the operation of a read-out link. Hence this LED was not considered to be failing.

| Device type | Particle | Fluence (10^{14} cm $^{-2}$) | Current during irradiation | Annealing current(s) (mA) | Annealing tempera- ture ($^{\circ}$ C) | Comments | | | | | |
|-------------------------------------|----------|-------------------------------------|----------------------------------|---------------------------------|--|--|-----|------------|----|-----|--|
| ABB Hafo LEDs | p | 0.7 | off | 10 | +10 | Ohmic resistor after the irradiation. Behaves like the other devices during the annealing, but the light output dropped after a three months storage period (see fig. 6.7.d). | | | | | |
| | n | 5.3 | off | 10 | +10 | | | | | | |
| GEC- Marconi LEDs | p | 2.2 | 18 mA pulsed | 80 | +10 | Yields a little light after the annealing and dies within 30 minutes of operation. Behaves like an ohmic resistor (see fig. 6.7.a and b). | | | | | |
| | | | | | | | 2.5 | 20 mA pul. | 50 | -10 | Low light output and almost no annealing. Slow annealing. |
| | | | | | | | 2.2 | 20 mA pul. | 50 | +10 | |
| VCSELs ($I_{th} \approx 2$ mA) | p | 1.8 | off | 4 | -10 | Does not yield any light after the irradiation. | | | | | |
| | | | | | | | 4.4 | off | 2 | -10 | Does yield some light after the irradiation, but dies during the first few measurements after the irradiation. |
| | | | | | | | 4.4 | off | 2 | -10 | |
| | | | | | | | 4.4 | off | 2 | +10 | |
| VCSELs ($I_{th} \lesssim 1$ mA) | n | 4.4 | off | 2 | -10 | Yields no light after the irradiation and the forward voltage is very low. | | | | | |
| | | | | | | | 4.4 | off | 2 | +10 | |
| | | | | | | | 4.4 | off | 2 | +10 | |
| | | | | | | | 4.4 | off | 2 | +10 | |

Table 7.2: Summary of failing devices irradiated with fluences between 2.0 and $8.1 \cdot 10^{14}$ n/cm 2 or between 0.6 and $2.5 \cdot 10^{14}$ p/cm 2 .

Chapter 8

Summary and Outlook

ATLAS is one of the two general purpose proton-proton experiments prepared for the Large Hadron Collider (LHC). Due to the very high luminosity operation of LHC, the inner detector of ATLAS will be subject to high fluences of neutral and charged particles. Therefore, all components to be used in the inner detector have to be tested on their radiation hardness and long term reliability.

In this work we have presented irradiation and life time studies of LEDs and VCSELs, which could be used as emitters in the optical links proposed for the read-out of the SemiConductor Tracker (SCT). In order to study both the short term annealing behavior and the life time after the irradiation of a large number of devices, an automatic measurement system (the scanning machine) was built, which allows for long term tests of several hundred LEDs and VCSELs.

In different irradiation runs about 120 and 130 LEDs manufactured by ABB Hafo and GEC-Marconi, respectively, and about 200 VCSELs produced by Sandia National Laboratories were irradiated with proton and neutron fluences as high as those expected during ten years of operation at LHC.

After irradiation with about $2 \cdot 10^{14}$ p/cm² and the subsequent annealing treatment at a forward current of 50 mA, which increased the light output considerably due to injection annealing, a relative light output of about 10 – 30% was found for the GEC-Marconi LEDs. For the ABB LEDs the relative light output after equivalent fluences is about 20 – 40%, while for VCSELs an almost complete annealing was observed.

At the time of this writing, the operating time reached in the life time studies is estimated to correspond to up to 45 years of operation at LHC. No devices failed during the high temperature operation, but 3 out of 58 GEC-Marconi and 3 out of 91 ABB Hafo LEDs gave less than 10% of the initial light output after the irradiation and the subsequent annealing treatment. These statistics include only devices irradiated with either a neutron fluence in the range from $2.0 \cdot 10^{14}$ n/cm² to $8.1 \cdot 10^{14}$ n/cm², or with a proton fluence in the range from $0.6 \cdot 10^{14}$ p/cm² to $2.5 \cdot 10^{14}$ p/cm². For LEDs an initial light output above 5 μ W was required for inclusion into the statistics.

Only one out of 126 VCSELs with a lasing threshold current above about 2 mA and irradiated with a fluence up to $3.7 \cdot 10^{14}$ p/cm² has failed. In contrary, for the

VCSELs with a threshold current below 1 mA six failures in a total 21 devices irradiated with $3.7 \cdot 10^{14}$ p/cm² or $4.4 \cdot 10^{14}$ n/cm² have been observed.

The results achieved have been used to estimate the performance of an optical link based on GEC-Marconi LEDs as presented in the Technical Design Report [8]. After ten years of operation at LHC an average S/N of 65 is expected for this type of link. Further experience with optical links will be gained during summer 1997 in the context of the Tracker System Prototyping (TSP) test beam program.

An attractive alternative to GEC-Marconi LEDs would be the use of Vertical Cavity Surface Emitting Laser diodes (VCSELs) yielding much more light and showing an astonishing radiation hardness. However, one major problem for the use of VCSELs concerns the packaging and the coupling of light from VCSELs to fibres. These issues will be studied by GEC-Marconi and Sandia National Laboratories specifically for the application at LHC.

Bibliography

- [1] LHC Study Group, *The Large Hadron Collider, Conceptual Design Report*, CERN/AC/95-05 (1995)
- [2] J. Beringer et al., *A life time test of neutron irradiated light emitting diodes*, Nucl. Instr. and Meth. **A373** (1996) 320
- [3] J. Beringer, *Studies for the Inner Detector of the ATLAS Experiment at the Large Hadron Collider*, PhD Thesis, University of Bern, 1996
- [4] ATLAS Collaboration, *Technical Proposal for a General-Purpose pp Experiment at the Large Hadron Collider at CERN*, CERN/LHCC/94-43 (1994)
- [5] CMS Collaboration, *The Compact Muon Solenoid — Technical Proposal*, CERN/LHCC/94-38 (1994)
- [6] LHC-B Collaboration, *Letter of Intent for A Dedicated LHC Collider Beauty Experiment for Precision Measurements of CP-Violation*, CERN/LHCC/95-5 (1995)
- [7] ALICE Collaboration, *Technical Proposal for a Large Ion Collider Experiment at the CERN LHC*, CERN/LHCC/95-71 (1995)
- [8] ATLAS Collaboration, *ATLAS Inner Detector Technical Design Report, Volume 2*, ATLAS TDR 5, CERN/LHCC/97-17 (1997)
- [9] M. Kyoto et al., *Gamma-Ray Irradiation Effect on Loss Increase of Single Mode Optical fibres, (II)*, J. Nucl. Sci. and Technology, vol. 26 (1989) 575
- [10] B. Dinkespiler et al., *Neutron Irradiation of Optical Link Components*, ATLAS Internal Note, LARG-NO-002 (1994)
- [11] RD-23 Collaboration, *Status Report on the RD-23 Project: Optoelectronic Analogue Signal Transfer for LHC Detectors*, LERB Status Report/RD23, CERN/LHCC/95-61 (1995)
- [12] K. Gill et al., *Ionising radiation of optical fibre data link components in the CMS Inner Tracker*, CMS TN/95-005 (1995)
- [13] S. Oglesby, Talk given at the SCT links meeting at CERN, February 27, 1997

- [14] T. Weidberg, private communication
- [15] V.A.J. van Lint, *The Physics of Radiation Damage in Particle Detectors*, Nucl. Instr. and Meth. **A253** (1987) 453
- [16] A.L. Barry et al., *An Improved Displacement Damage Monitor*, IEEE Trans. Nucl. Sci., vol. NS-37, no. 6 (1990) 1726
- [17] A.M. Ougouag et al., *Differential Displacement Kerma Cross Section for Neutron Interactions in Si and GaAs*, IEEE Trans. Nucl. Sci., vol. NS-37, no. 6 (1990) 2219
- [18] V.A.J. van Lint, R.E. Leadon and J.F. Colwell *Energy Dependence of Displacement Effects in Semiconductors*, IEEE Trans. Nucl. Sci., vol. NS-19, no. 6 (1972) 181
- [19] S. Wood et al., *Simulation of Radiation Damage in Solids*, IEEE Trans. Nucl. Sci., vol. NS-28, no. 6 (1981) 4107
- [20] G.P. Mueller, N.D. Wilsey and M. Rosen, *The Structure of Displacement Cascades in Silicon*, IEEE Trans. Nucl. Sci., vol. NS-29, no. 6 (1982) 1493
- [21] C.J. Dale et al., *Displacement damage equivalent to dose in silicon devices*, Appl. Phys. Lett., vol. 54, no. 5 (1989) 451
- [22] D.V. Lang, *Deep-level transient spectroscopy: A new method to characterize traps in semiconductors*, Appl. Phys. Lett., vol. 45, no. 7 (1974) 3023
- [23] M. Bosetti et al., *DLTS measurement of energetic levels, generated in silicon detectors*, Nucl. Instr. and Meth. **A361** (1995) 461
- [24] G.C. Messenger, *A Summary Review of Displacement Damage from High Energy Radiation in Silicon Semiconductors and Semiconductor Devices*, IEEE Trans. Nucl. Sci., vol. NS-39, no. 3 (1992) 468
- [25] C.J. Dale et al., *High Energy Electron Induced Displacement Damage in Silicon*, IEEE Trans. Nucl. Sci., vol. NS-35, no. 6 (1988) 1208
- [26] G.P. Summers et al., *Damage Correlations in Semiconductors Exposed to Gamma, Electron and Proton Radiations*, IEEE Trans. Nucl. Sci., vol. NS-40, no. 6 (1993) 1372
- [27] A.L. Barry et al., *The Energy Dependence of Lifetime Damage Constants in GaAs LEDs for 1–500 MeV Protons*, IEEE Trans. Nucl. Sci., vol. NS-42, no. 6 (1995) 2104
- [28] T.F. Luera et al., *Neutron Damage Equivalence for Silicon, Silicon Dioxide, and Gallium Arsenide*, IEEE Trans. Nucl. Sci., vol. NS-34, no. 6 (1987) 1557

-
- [29] G.P. Summers et al., *Correlation of Particle-Induced Displacement Damage in Silicon*, IEEE Trans. Nucl. Sci., vol. NS-34, no. 6 (1987) 1134
- [30] G.P. Summers et al., *Displacement Damage in GaAs Structures*, IEEE Trans. Nucl. Sci., vol. NS-35, no. 6 (1988) 1221
- [31] A. Chilingarov, J.S. Meyer and T. Sloan, *Radiation Damage due to NIEL in GaAs Particle Detectors*, ATLAS Internal Note, INDET-NO-134 (1996)
- [32] J. Lindhard et al., *Integral Equations Governing Radiation Effects*, Kgl. Dan. Vidensk. Selsk. Mat.-Fys. Medd., vol. 33, no. 10 (1963) 2
- [33] A. van Ginneken, *Non Ionizing Energy Deposition in Silicon for Radiation Damage Studies*, FERMILAB report FN-522 (1989)
- [34] M. Huhtinen and P.A. Aarnio, *Pion induced displacement damage in silicon devices*, Nucl. Instr. and Meth. **A335** (1993) 580
- [35] C.E. Barnes, *Radiation effects on light sources and detectors*, SPIE Vol. 541 Radiation Effects in Optical Materials (1985), p.138
- [36] B.H. Rose and C.E. Barnes, *Proton damage effects on light emitting diodes*, J. Appl. Phys. **53**(3) (1982) 1772
- [37] P.J. Drevinsky, A.R. Frederickson and D.W. Elsaesser, *Radiation-Induced Defect Introduction Rates in Semiconductors*, IEEE Trans. Nucl. Sci., vol. NS-41, no. 6 (1994) 1913
- [38] L.W. Aukerman et al., *Radiation Effects in GaAs*, J. Appl. Phys. **34**(63) (193590)
- [39] *HBOOK – Statistical Analysis and Histogramming*, CERN Program Library 1995
- [40] *PAW – Physics Analysis Workstation*, CERN Program Library 1995
- [41] M. Edwards and D.R. Perry, *The Radiation Hardness Test Facility*, Rutherford Appleton Laboratory, Oxon, England, 1990
- [42] M. Edwards, private communication
- [43] <http://www.cdn-news.com/DATABASE/ARCHIVE/1996/3/29/MLT0329.html>
- [44] T. Weidberg, private communication
- [45] P.L. Gourley, K.L. Lear and R.P. Schneider Jr., *Surface-emitting lasers*, IEEE Specturm, Volume 31, Number 8, August 1994
-

- [46] B. Dinkespiler et al., *Analogue Optical Links for the Front-End Read Out of the ATLAS Liquid Argon Calorimeter*, Proceedings of the 2nd Workshop of Electronics for LHC Experiments, Balatonfüred, Hungary, 1996, CERN/LHCC/96-39
- [47] E. Monnier, private communication
- [48] K.L. Lear, private communication
- [49] T.E. Sale, *Vertical Cavity Surface Emitting Lasers*, John Wiley & Sons Inc., New York 1995
- [50] K.D. Choquette et al., *Fabrication and Performance of Selectively Oxidized Vertical-Cavity Lasers*, IEEE Photonics Techn. Letters, vol. 7, no. 11 (1995)
- [51] J.K. Guenter et al., *Reliability of proton-implanted VCSELs for data communications*, Proceedings of the SPIE, vol. 2683, pp. 102-113, SPIE, San Jose, CA (1996)
- [52] M. Osiński and W. Nakwaski, *Thermal Effects in Vertical-Cavity Surface-Emitting Lasers*, Intern. J. of High Speed Electr. and Systems, vol 5, no. 4, p. 667-730 (1994)
- [53] Y.A. Akulova et al., *Low-Temperature Optimized Vertical-Cavity Lasers with Submilliamp Threshold Currents over the 77-370K Temperature Range*, IEEE Photonics Techn. Letters, vol. 9, no. 3 (1997)
- [54] S. Jiang, M. Dagenais and R.A. Morgan, *Spectral Characteristics of Vertical-Cavity Surface-Emitting Lasers with Strong External Optical Feedback*, IEEE Photonics Techn. Letters, vol. 7, no. 7 (1995)
- [55] D.M. Kuchta et al., *Relative intensity noise of vertical cavity surface emitting lasers*, Appl. Phys. Lett., vol. 62, no. 11 (1993) 1194
- [56] C.J. Chang-Hasnain et al., *Dynamic, Polarization, and Transverse Mode Characteristics of Vertical Cavity Surface Emitting Lasers*, IEEE J. of Quantum Electronics, vol. 27, no. 6 (1991)
- [57] D. Vakhshoori et al., *Top-surface emitting lasers with 1.9V threshold voltage and the effect of spatial hole burning on their transverse mode operation and efficiencies*, Appl. Phys. Lett., vol. 62, no. 13 (1993) 1448
- [58] G.C. Wilson et al., *Spatial hole burning and self-focusing in vertical-cavity surface-emitting laser diodes*, Appl. Phys. Lett., vol. 64, no. 5 (1994) 542
- [59] A. Valle, J. Sarma and K.A. Shore, *Spatial Holeburning Effects on the Dynamics of Vertical Cavity Surface-Emitting Laser Diodes*, IEEE J. of Quantum Electronics, vol. 31, no. 8 (1995)

- [60] L. Raddatz et al., *Measurement of Guiding Effects in Vertical-Cavity Surface-Emitting Lasers*, IEEE Photonics Techn. Letters, vol. 8, no. 6 (1996)
- [61] Y. Kaneko et al., *Transverse-mode characteristics of InGaAs/GaAs vertical-cavity surface-emitting lasers considering gain offset*, Japn. J. Appl. Phys., vol. 32, p. L1612 (1993)
- [62] D.L. Huffaker et al., *Improved mode stability in low threshold single quantum well native-oxide defined vertical-cavity lasers*, Appl. Phys. Lett., vol. 65, no. 21 (1994) 2642
- [63] T.J. Rogers et al., *Influence of Cavity Tuning on the Transverse Mode in Vertical-Cavity Lasers*, IEEE Photonics Techn. Letters, vol. 7, no. 3 (1995)
- [64] M. Leiby et al., *Use of VCSEL Arrays for Parallel Optical Interconnects*, Proceedings of the SPIE, vol. 2683, pp. 81–91, SPIE, San Jose, CA (1996)
- [65] H. Kosaka et al., *2D alignment free VCSEL-array module with push/pull fibre connector*, Electr. Lett., vol. 32, no. 21 (1996)
- [66] M. Kajita et al., *1-Gb/s Modulation Characteristics of a Vertical-Cavity Surface-Emitting Laser Array Module*, IEEE Photonics Techn. Letters, vol. 9, no. 2 (1997)
- [67] J. Wilson, Talk given at the SCT links meeting at CERN, December 18, 1996
- [68] I. Dawson et al., *Irradiation Tests of Optoelectronic Components for ATLAS SCT Readout*, ATLAS Internal Note, INDET-NO-137 (1996)
- [69] M.H. Pilkuhn, *Light Emitting Diodes*, in ed. T.S. Mose, *Handbook on Semiconductors*, volume 4, North-Holland (1981)
- [70] Honeywell, *Long-Term Power Output Reliability of Cap Rock (SEC589) LED Chip*, Optoelectronics Fiber Optic Products, Catalog E27 (1993)
- [71] Hewlett Packard, *Reliability Considerations in Designing Fiber Optic Transmitters*, Optocoupler and Fiber Optics Applications Handbook (1986)

Acknowledgments

I would like to thank all friends and colleagues who have made their contribution to this work. In particular I would like to thank:

- Prof. Dr. K. Pretzl for the opportunity to participate in the exciting and interesting ATLAS experiment;
- Jürg Beringer for his friendly collaboration and guidance, for many interesting discussions and for the good time spent together during the LED/VCSEL life time studies;
- Kurt Borer for the nice teamwork and for his advice;
- Richard Nickerson and Tony Weidberg for their collaboration concerning the LED/VCSEL life time studies;
- Bob Kowalewski and the SCT links community for valuable informations;
- Vera Dvorak, Max Hess, Simon Lehmann, Jean-Claude Roulin, Helmut Ruetsch, and Hans-Ulrich Schütz for providing and supporting the electronics and mechanics required for the scanning machine;
- Kevin Lear and Emmanuel Monnier for providing the VCSELs and for interesting discussions;
- Maurice Glaser, François Lemeilleur and their team for doing the proton irradiations at the PS facility;
- Mike Edwards and his team for doing the neutron irradiation at the ISIS facility;
- All the colleagues from the NA52 experiment giving me the opportunity to participate in a running experiment;
- Michele Weber and Anita Finger for many pleasant hours spent together;
- Phil Annen, Lea Bennett, Matthias, Esther and Julian Bigler, Theo Fröhlich, Roger Grandjean, Regine Röthlisberger, and Luca Weber as well as the former inhabitants of the 9th floor of the Tscharni for uncountable memories of my student time.

Last but not least, I am deeply indebted to my grand mother Tiny Straub and my friend Dona Ghosh for their love, their support, and their considerations during busy times.

